J. Fluid Mech. (2026), *vol.* 1030, A52, doi:10.1017/jfm.2026.11229

Triangular instability of a strained Batchelor vortex

Aditya Sai Pranith Ayapilla[1,†], **Yuji Hattori**[2] **and Stéphane Le Dizès**[3]

[1]Graduate School of Information Sciences, Tohoku University, Sendai 980-8579, Japan
[2]Institute of Fluid Science, Tohoku University, Sendai 980-8577, Japan
[3]Aix Marseille Université, Centrale Méditerranée, IRPHE, CNRS, Marseille France
Corresponding author: Aditya Sai Pranith Ayapilla, ayapilla.aditya.sai.pranith.t6@dc.tohoku.ac.jp

(Received 27 June 2025; revised 26 November 2025; accepted 18 January 2026)

We investigate the triangular instability of a Batchelor vortex subjected to a stationary triangular strain field generated by three satellite vortices, in the presence of weak axial flow. The analysis combines theoretical predictions with numerical simulations. Theoretically, the instability arises from resonant coupling between two quasi-neutral Kelvin modes with azimuthal wavenumbers m and $m+3$ with the background strain. Numerically, we solve the linearised Navier–Stokes equations around a quasi-steady base flow to identify the most unstable modes, and compare their growth rates and frequencies with theoretical predictions for a Reynolds number $\mathrm{Re}=10^4$ and a straining strength $\epsilon=0.008$. In the absence of axial flow, only the mode pair $(m_A, m_B)=(-1, 2)$ (and its symmetric counterpart) is unstable. However, we show that additional combinations such as $(0, 3)$, $(1, 4)$ and $(2, 5)$, which are otherwise strongly damped by the critical layer in the absence of axial flow, also become unstable once axial flow exceeds a certain threshold, as the critical-layer damping is significantly reduced. Furthermore, we show that the most unstable mode in the no-axial-flow case, originating from the second branch of $m=-1$ and the first branch of $m=2$, becomes less unstable as axial flow increases. It is eventually overtaken by a mode from the first branches of both wavenumbers, which then remains the dominant unstable mode across a wide range of axial flow strengths, Reynolds numbers and straining strengths. A comprehensive instability diagram as a function of the axial flow parameter is presented.

Key words: vortex instability, wakes, critical layers

[†] *Current Address:* Supercomputing Research Center, Institute of Integrated Research, Institute of Science Tokyo, Tokyo 152-8550, Japan

1. Introduction

Vortices are naturally prone to instabilities triggered by small disturbances, which can amplify through inviscid or viscous mechanisms either within the vortex core or via interactions with the surrounding flow. Understanding vortex stability is of great theoretical interest and practical importance across a wide range of natural and industrial flows, including geophysical and astrophysical systems, aircraft wakes and various rotating flows. A detailed overview of vortex stability theory can be found in Ash, Khorrami & Green (1995).

Among the various types of instabilities, short-wave instabilities occur at scales comparable to or smaller than the vortex core. These arise through parametric resonance, where two Kelvin modes of the underlying vortex become resonant with the vortex correction induced by the background strain. Depending on the nature of the background strain, two well-studied types of short-wave instabilities are: (i) the elliptic instability, where the strain induces a quadrupolar correction that causes elliptic deformation of the vortex streamlines; and (ii) the curvature instability, where a dipolar correction is introduced. The elliptic instability is a key mechanism by which vortex pairs, such as wingtip vortices of aeroplanes, develop instabilities, alongside the Crow instability (Crow 1970; Leweke, Le Dizès & Williamson 2016). In such cases, each vortex induces a quadrupolar correction on its counterpart, leading to elliptic bending of streamlines and the onset of elliptic instability. In contrast, curvature instability typically arises from the bending of vortex tubes, such as in curved filaments and vortex rings, where the curvature creates a dipolar correction. Moore & Saffman (1975) and Tsai & Widnall (1976) were the first to explain this mechanism as a parametric resonance, for the Lamb–Oseen vortex and Rankine vortex, respectively. A thorough summary of the elliptic instability is provided by Kerswell (2002), with notable contributions from Pierrehumbert (1986), Bayly (1986), Leweke & Williamson (1998), Le Dizes & Laporte (2002), Meunier & Leweke (2005), Schaeffer & Le Dizès (2010), Blanco-Rodríguez & Le Dizès (2016), Lacaze, Ryan & Le Dizès (2007) among others. Curvature instability was first observed in a helical vortex filament by Widnall (1972), along with long-wave and mutual-inductance instability modes. Further theoretical and numerical studies on vortex rings and helical vortices include works by Hattori & Fukumoto (2003), Fukumoto & Hattori (2005), Blanco-Rodríguez & Le Dizès (2017), Hattori, Blanco-Rodríguez & Le Dizès (2019), Xu *et al.* (2025) among others.

Multipolar short-wave instabilities, involving strain of order higher than two or non-axisymmetric vortices with higher symmetries, have received comparatively little attention. Long-lived non-axisymmetric vortices – such as dipoles, tripoles and higher-order multipoles – have been observed in rotating turbulent flows through experiments and simulations (Hopfinger & Van Heijst 1993; Carnevale & Kloosterziel 1994; Rossi, Lingevitch & Bernoff 1997; Dritschel 1998). There is also evidence of Kelvin waves emerging on vortex filaments in transitional flows (Arendt, Fritts & Andreassen 1998), with elliptic and multipolar instabilities potentially explaining their appearance and providing a mechanism for rich vortex dynamics of turbulent flows and transition. Multipolar instability has been studied theoretically and numerically for Rankine vortices (Le Dizès & Eloy 1999; Le Dizes 2000; Eloy & Le Dizès 2001), with experimental evidence of triangular instability reported in rotating cylinder configurations (Eloy *et al.* 2000, 2003). However, Rankine vortices are idealised, whereas models with continuous vorticity distributions, such as Lamb–Oseen and Batchelor vortices – self-similar solutions of the Navier–Stokes equations – offer a more realistic representation of vortices in wakes and rotating flows, with multipolar instability particularly having potential implications in rotor wakes such as wind turbines and ship propellers. This highlights the importance of studying multipolar instabilities in these models. Additionally, continuous vorticity profiles give rise to critical layers, which suppress many Kelvin modes and significantly affect instability behaviour (Sipp & Jacquin 2003; Fabre & Jacquin 2004; Le Dizès 2004; Le Dizès & Lacaze 2005; Fabre, Sipp & Jacquin 2006).

In a recent study (Ayapilla, Hattori & Le Dizès 2025), we presented the first evidence of triangular instability in a Lamb–Oseen vortex and characterised its behaviour both theoretically and numerically. For brevity, we refer to Ayapilla *et al.* (2025) as AHL25. However, it is important to extend this analysis to the Batchelor vortex. In reality, vortices in wakes often possess a non-zero axial flow component, and the Batchelor vortex is recognised as a better model for trailing vortices in aircraft wakes (Batchelor 1964). Rotor wakes such as in Joukowski's rotor wake model, typically consist of a hub vortex, root vortices and tip vortices, where the hub vortex generally possesses axial flow. Therefore, investigating the effect of axial flow on the triangular instability is crucial. The influence of axial flow on the elliptic instability has been examined for a Rankine vortex by Lacaze, Birbaud & Le Dizès (2005) and for the Batchelor vortex by Lacaze *et al.* (2007). These works showed that adding a small axial flow slightly modifies the dispersion curves and breaks the symmetry between Kelvin modes, leading to new resonant modes and altering how the critical layer affects the modes. For example, beyond the well-known stationary helical modes $m = 1$ and -1 in the elliptic instability of the Lamb–Oseen vortex, modes with $m = 0$, 2, and other pairs were also shown to become unstable. The asymptotic behaviour of the Kelvin modes of the Batchelor vortex with small axial flow, in the large axial wavenumber limit, was analysed using a Wentzel–Kramers–Brillouin (WKB) approach by Le Dizès & Lacaze (2005). The effects of axial flow on curvature instability have been studied in various configurations: for a helical vortex tube by Hattori & Fukumoto (2012, 2014), for a curved Batchelor vortex by Blanco-Rodríguez & Le Dizès (2017) and in a vortex ring with swirl by Hattori *et al.* (2019), using numerical stability analysis.

The unstrained Batchelor vortex (or q vortex) can become unstable when the axial flow is sufficiently strong (see Ash *et al.* (1995) for a review). Inviscid unstable modes were first computed numerically by Lessen, Singh & Paillet (1974) for swirl parameters $q < 1.5$, which corresponds to an axial flow parameter $W_0 > 0.66$. Leibovich & Stewartson (1983) later derived a sufficient condition for inviscid instability given by $q < \sqrt{2}$. Extending this further, Heaton (2007) demonstrated that weakly unstable inviscid modes can exist up to $q \approx 2.31$, i.e. for $W_0 > 0.43$. The Batchelor vortex also supports unstable viscous modes. These were first identified by Khorrami (1991), and later, a distinct class known as viscous centre modes localised near the vortex axis was obtained by Fabre & Jacquin (2004) for low swirl values. An asymptotic description of these modes was provided by Le Dizès & Fabre (2007), where the authors showed that the Batchelor vortex becomes unstable for any positive axial flow if the Reynolds number is sufficiently high. The full stability curve was further analysed by Fabre & Le Dizès (2008), who derived an expression for the critical swirl number as a function of Reynolds number, below which viscous centre modes become unstable. These asymptotic results will later be used in this work to analyse the competition between the viscous instability of the unstrained Batchelor vortex and the triangular instability of the strained vortex.

Capitalising on this motivation, our objective in this study is to investigate how axial flow influences the triangular instability of a strained Batchelor vortex. In AHL25 we demonstrated that the triangular instability in the Lamb–Oseen vortex was restricted to the azimuthal wavenumber pair $m = 1$ and -2 (or $m = -1$ and 2). Here, we expect this picture to change with the inclusion of small axial flow, which is the focus of the present investigation. We restrict attention to small axial flow values to ensure that triangular instability modes, if present, can become more unstable than the inviscid or the viscous centre modes previously discussed. As in AHL25, we adopt a combined approach of theoretical linear stability analysis and numerical stability analysis based on linearised direct numerical simulations, hereafter referred to simply as DNS. In the DNS framework, we first compute the base flow and then solve the linearised Navier–Stokes equations about that base flow to identify the most unstable mode. The theoretical framework involves deriving an approximate base flow under the assumption of a weak triangular straining field and using it to formulate the linear perturbation equations for the strained Batchelor vortex. These equations are then used to calculate the growth rates of the resonant modes. To identify these resonant modes, we solve the eigenvalue problem for the unperturbed vortex.

The paper is structured as follows. Section 2 describes the numerical framework, beginning with the flow set-up in § 2.1, followed by the governing equations for the base flow and linear stability analysis, and the numerical procedure in § 2.2. We then present the details of the numerical simulations and theoretical formulation of the base flow in § 3, introduce the perturbation equations and define the resonance condition for triangular instability in § 4. Section 5 examines the Kelvin modes of the Batchelor vortex. In § 5.1 we outline the numerical approach for computing the Kelvin modes of the unstrained vortex. In § 5.2 we classify Kelvin modes using the large-k asymptotic framework of Le Dizès & Lacaze (2005) and identify the resonance domain in which triangular instability can arise. Section 6 analyses the characteristics of triangular instability. We first derive the theoretical growth rate expression for resonant modes in § 6.1. In § 6.2 we compare and validate the numerically obtained unstable modes, including their growth rates, against the theoretical predictions for selected axial flow values. In § 6.3 we use the theoretical framework to conduct a parametric study exploring how the instability characteristics vary with axial flow, Reynolds number and straining strength. Finally, § 7 summarises the main findings and discusses potential directions for future work.

2. Numerical methodology

Let us recall that the numerical analysis consists of two main steps. First, we compute the quasi-steady base flow by solving the incompressible Navier–Stokes equations. Then for the linear stability analysis, we integrate the linearised Navier–Stokes equations around this base flow over a sufficiently long time to identify the most unstable mode, if one exists, for a specified axial wavenumber.

The framework for carrying out numerical simulations, including flow set-up, numerical methods, initial conditions and simulation parameters are almost identical to those used in AHL25, with the key difference being that the current set-up includes axial flow. Below, we delve into the specific details and after formulating the flow set-up, we present the governing equations discretised and the numerical procedure used for the base flow and linear stability analysis.

2.1. *Flow set-up*

We consider the problem in a cylindrical coordinate system (r, θ, z). The initial configuration consists of a central hub Lamb–Oseen vortex located at $r = 0$, symmetrically surrounded by three satellite Lamb–Oseen vortices in an incompressible, viscous fluid, as shown in figure 1 in the r–θ plane. The three satellite vortices are located at a distance R from the hub, separated by an angle of $2\pi/3$. Since the hub vortex is now assumed to have an axial flow in the z direction with a Gaussian profile, as illustrated in figure 1, it is modelled as a Batchelor vortex. The satellite vortices are modelled as Lamb–Oseen vortices and impose a triangular straining field on the hub vortex. The two-dimensional

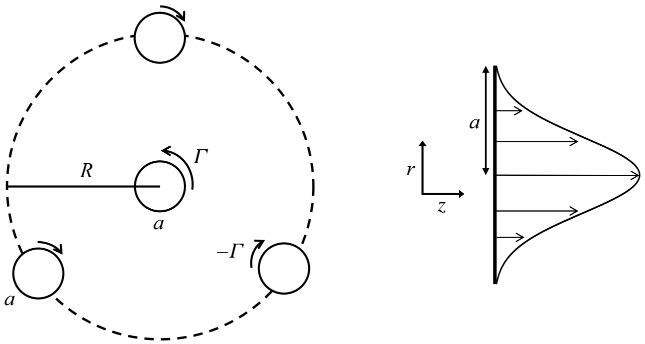

Figure 1. Flow configuration of the hub vortex and the three satellite vortices.

(2-D) vorticity distribution $\zeta_0(r)$ for all the vortices is therefore taken as

$$\zeta_0(r) = \frac{\varGamma_i}{\pi a_i^2} \exp\left(-\frac{|r-r_c|^2}{a_i^2}\right), \tag{2.1}$$

where a_i is the initial radius of a vortex, $\varGamma_i$ is the initial circulation and r_c is the radial location of the vortex centre.

The axial velocity component $\overline{W}_0(r)$ of the Batchelor hub vortex is taken as

$$\overline{W}_0(r) = W_{0,i} \exp\left(-\frac{r^2}{a_i^2}\right), \tag{2.2}$$

where $W_{0,i}$ is a free parameter that represents the strength of the axial flow. The subscript i indicates that it corresponds to the initial state of the system. It is related to the swirl number S – defined as the ratio of the maximum azimuthal to axial velocity – by $W_{0,i} = 0.638/S$ (Lessen *et al.* 1974).

The Reynolds number of the flow Re, is defined as

$$Re = \frac{\varGamma_i}{2\pi \nu}, \tag{2.3}$$

where ν is the kinematic viscosity.

2.2. *Governing equations, domain and discretisation*

The governing equations for both the base flow and linear stability analysis are derived from the three-dimensional incompressible Navier–Stokes equations in cylindrical coordinates (r, θ, z) for the velocity field $\boldsymbol{U} = (U, V, W)$ and pressure P given by

$$\frac{\partial U}{\partial t} = -U\frac{\partial U}{\partial r} - \frac{V}{r}\frac{\partial U}{\partial \theta} - W\frac{\partial U}{\partial z} + \frac{V^2}{r} - \frac{\partial P}{\partial r} + \nu\left[\left(\nabla^2 - \frac{1}{r^2}\right)U - \frac{2}{r^2}\frac{\partial V}{\partial \theta}\right], \tag{2.4}$$

$$\frac{\partial V}{\partial t} = -U\frac{\partial V}{\partial r} - \frac{V}{r}\frac{\partial V}{\partial \theta} - W\frac{\partial V}{\partial z} - \frac{UV}{r} - \frac{1}{r}\frac{\partial P}{\partial \theta} + \nu\left[\left(\nabla^2 - \frac{1}{r^2}\right)V + \frac{2}{r^2}\frac{\partial U}{\partial \theta}\right], \tag{2.5}$$

$$\frac{\partial W}{\partial t} = -U\frac{\partial W}{\partial r} - \frac{V}{r}\frac{\partial W}{\partial \theta} - W\frac{\partial W}{\partial z} - \frac{\partial P}{\partial z} + \nu\nabla^2 W, \tag{2.6}$$

$$\frac{\partial U}{\partial r} + \frac{U}{r} + \frac{1}{r}\frac{\partial V}{\partial \theta} + \frac{\partial W}{\partial z} = 0. \tag{2.7}$$

2.2.1. *Base flow*

It is important to note that although the base flow includes an axial velocity component, none of the three velocity components exhibit any variation along the axial (z) direction. The axial flow is therefore decoupled from the dynamics of the other two velocity components, and the evolution of the flow in the r–θ plane and z direction are independent of each other. Accordingly, the governing equations are obtained by setting all partial derivatives with respect to z in (2.4)–(2.7) to zero, and the resulting system is solved numerically.

The computational grid for the base flow is constructed in two dimensions, with discretisation performed only in the radial and azimuthal directions. A sixth-order compact finite difference scheme (Lele 1992) is used in r, and a Fourier spectral method is employed in θ, with periodic boundary conditions. The numerical domain spans $-1000 \leqslant r \leqslant 1000$, with the grid extended to negative r to avoid the singularity at $r = 0$. As will be shown in § 3, the hub–satellite vortex system is confined to $r < 10$; nevertheless, a large radial extent of 1000 is adopted to ensure numerical convergence. To keep the computation efficient, a non-uniform radial grid is adopted, using 695 points with a fine grid spacing of 0.0475 near the vortices and a coarser spacing farther away. In the azimuthal direction, 512 Fourier modes are used. The Poisson equation for pressure is decomposed into a set of ordinary differential equations for each Fourier mode and solved using the same sixth-order compact scheme. For temporal discretisation, the Crank–Nicolson scheme is applied to the viscous terms, while the second-order Adams–Bashforth method is used for the remaining terms. Further details on numerical methods and how the accuracy of the numerical simulations depends on the grid resolution are provided in Appendices A and B, respectively, of Hattori *et al.* (2019).

2.2.2. *Linear stability analysis*

The linearised DNS, on the other hand, is extended to three dimensions (r, θ, z), where a single normal mode with a specified axial wavenumber is considered in the z direction. Specifically, if the base flow is $[U(r,\theta), V(r,\theta), W(r,\theta)]$, then the linearised Navier–Stokes equations about the base flow for disturbances u', v', w' and p', which are functions of r, θ and z, are given by

$$\begin{aligned}\partial u' t = {} & -U\partial u' r - \frac{V}{r}\partial u'\theta - W\partial u' z + \frac{2Vv'}{r} - u'\partial U r - \frac{v'}{r}\partial U\theta \\ & - \partial p' r + \frac{1}{Re}\left[\left(\nabla^2 - \frac{1}{r^2}\right)u' - \frac{2}{r^2}\partial v'\theta\right],\end{aligned} \tag{2.8}$$

$$\begin{aligned}\partial v' t = {} & -U\partial v' r - \frac{V}{r}\partial v'\theta - W\partial v' z - u'\partial V r - \frac{v'}{r}\partial V\theta - \frac{Uv' + u'V}{r} \\ & - \frac{1}{r}\partial p'\theta + \frac{1}{Re}\left[\left(\nabla^2 - \frac{1}{r^2}\right)v' + \frac{2}{r^2}\partial u'\theta\right],\end{aligned} \tag{2.9}$$

$$\partial w' t = -U\partial w' r - \frac{V}{r}\partial w'\theta - W\partial w' z - u'\partial W r - \frac{v'}{r}\partial W\theta - \partial p' z + \frac{1}{Re}\nabla^2 w', \tag{2.10}$$

where $\nabla^2 = \partial_r^2 + (1/r)\partial_r + (1/r^2)\partial_\theta^2 + \partial_z^2$. These equations are discretised and solved numerically on the same $(r - \theta)$ grid as the base flow. The single wave in the z direction is represented by assuming periodic boundary conditions as

$$F(t, r, \theta, z) = \mathrm{e}^{\mathrm{i}kz} \sum_m \hat{F}_m(t, r)\mathrm{e}^{\mathrm{i}m\theta} \tag{2.11}$$

for the disturbance fields u, v, w and p, and thus rendering the equations separable in z. The same temporal discretisation as the base flow is used.

3. Base flow

3.1. *Numerical simulations*

This section outlines the initial conditions and flow parameters used in the numerical simulations to obtain the quasi-steady state of the system, which then serves as the base flow for the subsequent linearised simulations. We restrict our analysis to a non-rotating reference frame, and to achieve this, we assign the initial circulation of the hub vortex to be equal and have opposite sign to those of satellite vortices. So for the hub vortex, we take $\varGamma_i = \varGamma = 2\pi$. The circulation of each satellite vortex is thus set to -2π. This choice ensures that the net induced velocity at the centre of any vortex due to the others vanishes (negligible, although not perfectly zero), allowing the vortex system to remain stationary. We set $\mathrm{Re} = 1000$. Note that the quasi-steady state is anyway not expected to depend on the Reynolds number (Le Dizès & Verga 2002) and we chose a lower value of Reynolds number to ensure that the quasi-steady state is reached more rapidly. Under these conditions, the system consisting of the hub and satellite vortices evolves toward a quasi-steady state once all vortices reach equilibrium under their mutual interaction. We reiterate that the relaxation mechanism is identical to that of the Lamb–Oseen case, since the dynamics in the 2-D plane are independent of the axial flow. The axial velocity field also evolves independently according to the same governing equation as the axial vorticity, with the axial flow strength $W_{0,i}$ as the only varying parameter. Consequently, the axial flow reaches its quasi-steady state in the same manner as the planar flow field. For verification of the quasi-steady state, we refer the reader to § 3 (figures 4 and 5) of AHL25 and do not repeat it here.

The initial core radii of both the hub and satellite vortices, a_i, gradually increase during the relaxation process, stabilising at a larger value a given as

$$a^2(t) = a_i^2 + 4\nu t. \tag{3.1}$$

We begin the simulations with a core radius of $a_i = 0.8$ for both hub and satellite vortices, and terminated it when the core radius of the hub vortex reaches $a = 1$, which occurs after the quasi-steady state is established. The value of $a = 1$ is used to non-dimensionalise all spatial quantities in the theoretical analysis, presented in the next section. The distance between the hub and satellite vortices is set to $R = 5$, and it remains nearly constant throughout the relaxation process. Therefore, at the quasi-steady state, we have $a = 1$, $R = 5$, and at the leading order, the axial vorticity and the axial velocity of the hub vortex take the form

$$\zeta_0 = 2\mathrm{e}^{-r^2}, \tag{3.2}$$

$$\overline{W}_0 = W_0\mathrm{e}^{-r^2}. \tag{3.3}$$

The initial axial flow strength $W_{0,i}$ is set so that a desired target W_0 is achieved at the quasi-steady state.

3.2. *Theoretical description*

This section outlines the theoretical formulation of the base flow. While the numerical simulations account for the full configuration – including the hub vortex and the three satellite vortices – the theoretical analysis focuses solely on the hub vortex. The goal is to derive an approximate expression for the hub vortex's velocity field influenced by the surrounding satellites. We omit the full derivation and refer the reader to § 3 of AHL25 and earlier works by Moffatt, Kida & Ohkitani (1994), Jiménez *et al.* (1996) and Le Dizès (2000).

An asymptotic approximation of the base flow velocity field is obtained in the limit of small a/R by modelling the satellite vortices as line vortices, introducing the small parameter $\epsilon = (a/R)^3$. For the quasi-steady values of a and R in our set-up, this gives $\epsilon = 0.008$. In practical applications such as wind turbines and marine propellers, the ratio of the hub radius to the blade length, a/R, typically lies in the range 0.05–0.2. Moreover, the effective hub-vortex radius may be even larger in practice, as it forms through the merging of vortices generated near the blade roots. In contrast, tip vortices are substantially smaller – often of the order of $1/100$ of the blade length or even less – which further justifies the use of a line-vortex approximation for modelling the tip vortices. Overall, it can be reasonably argued that the value $\epsilon = 0.008$ lies within a realistic range for practical rotors and is sufficiently large to serve as a useful starting point for investigating triangular instability from a theoretical perspective.

The velocity field $(\overline{U}, \overline{V}, \overline{W})$ and the vorticity field ζ for the triangularly strained Batchelor vortex can be approximated as

$$\overline{U}(r, \theta) = \epsilon \frac{3f(r)}{r} \cos 3\theta + O\left(\epsilon^2\right), \tag{3.4}$$

$$\overline{V}(r, \theta) = r\varOmega_0(r) - \epsilon f'(r) \sin 3\theta + O\left(\epsilon^2\right), \tag{3.5}$$

$$\overline{W}(r, \theta) = \overline{W}_0 + \epsilon \overline{W}_1 + O\left(\epsilon^2\right), \tag{3.6}$$

$$\zeta(r, \theta) = \zeta_0 + \epsilon \zeta_1 + O\left(\epsilon^2\right), \tag{3.7}$$

where

$$\overline{W}_0 = W_0 \mathrm{e}^{-r^2}, \tag{3.8}$$

$$\overline{W}_1 = \frac{W_0}{2} g(r) \sin 3\theta, \tag{3.9}$$

$$\zeta_0 = 2\mathrm{e}^{-r^2}, \tag{3.10}$$

$$\zeta_1 = g(r) \sin 3\theta \tag{3.11}$$

and

$$g(r) = \frac{4r^2 f(r)}{1 - \mathrm{e}^{r^2}}. \tag{3.12}$$

Here, $\varOmega_0(r)$ denotes the angular velocity, given by $\varOmega_0(r) = (1 - \mathrm{e}^{-r^2})/r^2$, and $f(r)$ satisfies the second-order linear ordinary differential equation

$$f'' + r^{-1} f' - \left(9r^{-2} + \frac{4r^2}{(1 - \mathrm{e}^{r^2})}\right) f = 0, \tag{3.13}$$

with the boundary conditions

$$f(r) \sim s_0 r^3 \quad \text{at } r \to 0, \tag{3.14}$$

$$f(r) \sim r^3 \quad \text{at } r \to \infty. \tag{3.15}$$

The constant $s_0 \approx 1.7724$ appearing in these equations is a numerical constant derived from the integration of (3.13). It corresponds to the amplitude of the straining field in the vortex centre, normalised by the amplitude of the straining field at the same point in the absence of the vortex.

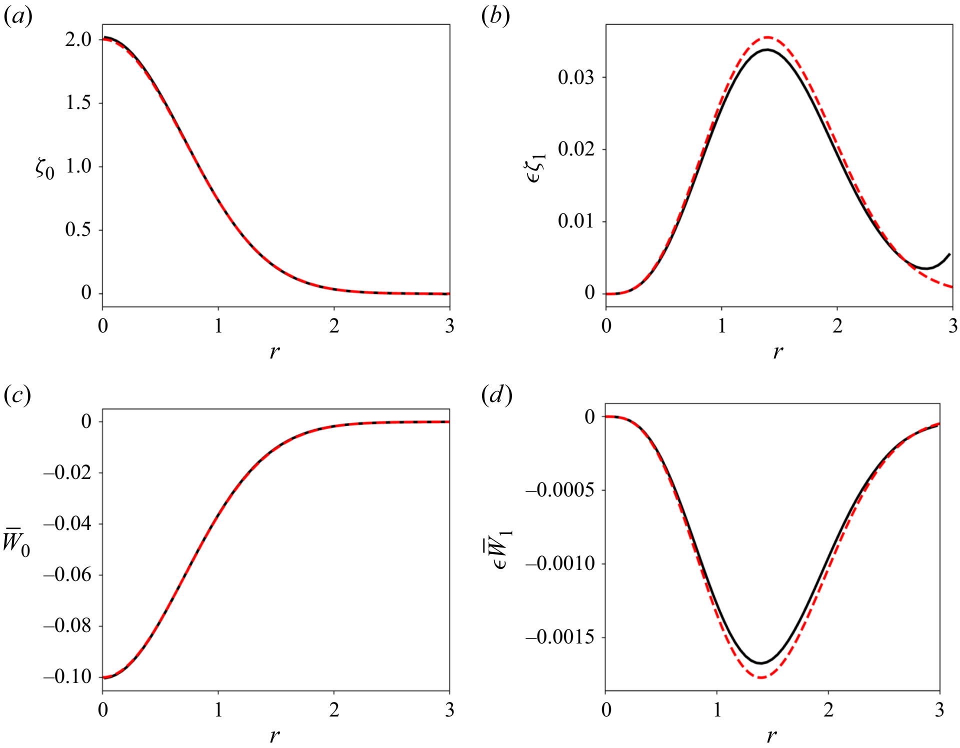

Figure 2. Comparison of the axial vorticity and axial velocity of the quasi-steady base flow obtained from DNS (solid black line) and theory (red dashed line) for $\mathrm{Re} = 1000$ and $\epsilon = 0.008$. Panels (*a*) and (*b*) show the leading-order term and the triangular straining correction of the axial vorticity, respectively. Panels (*c*) and (*d*) present the corresponding leading-order and correction terms for the axial velocity.

Next, we briefly compare and validate the numerically obtained base flow against the theoretical prediction. Figure 2 shows a comparison of the axial vorticity and axial velocity at the quasi-steady state from DNS and theory. The agreement is excellent, further confirming that the 2-D flow and the axial flow evolve independently while obeying the same governing equations. For this example, $W_{0,i}$ was chosen such that the quasi-steady value becomes $W_0 = -0.1$, although, as noted earlier, $W_{0,i}$ may be freely selected to achieve any desired W_0 at the quasi-steady state. Panels (*a*) and (*b*) of figure 2 correspond to the same results presented in figure 5 of AHL25. Finally, we note that in figure 2(*b*) the increase in the numerically obtained correction term of the vorticity near $r \approx 3$ arises from the presence of the satellite vortices. No such feature appears in panel (*d*), since no axial flow is imposed on the satellite vortices.

4. Linear perturbation equations and triangular instability mechanism

Using (3.4)–(3.6) for the base flow, the linearised Navier–Stokes equations for the velocity–pressure field $\boldsymbol{u} = (u, v, w, p)$ of the perturbations can be written in the form

$$\left(\mathcal{L}\frac{\partial}{\partial t} + \mathcal{P}\frac{\partial}{\partial z} + \mathcal{M} - \frac{\mathcal{V}}{Re}\right)\boldsymbol{u} = \epsilon\left(\mathrm{e}^{3\mathrm{i}\theta}\mathcal{N} + \mathrm{e}^{-3\mathrm{i}\theta}\overline{\mathcal{N}}\right)\boldsymbol{u}, \tag{4.1}$$

where the matrices $\mathcal{L}$, $\mathcal{P}$, $\mathcal{M}$, $\mathcal{V}$, $\mathcal{N}$ are given in Appendix A.

The mechanism for the growth of perturbations is due to the resonance of two quasi-neutral Kelvin modes of the Batchelor vortex with the triangular strain field. The Kelvin modes can be expressed as

$$\boldsymbol{u} = \tilde{\boldsymbol{u}}(r)\mathrm{e}^{\mathrm{i}(m\theta + kz - \omega t)}, \tag{4.2}$$

where m is the azimuthal wavenumber, k the axial wavenumber, ω the frequency and $\tilde{\boldsymbol{u}}(r)$ the eigenfunction field of the Kelvin mode. They satisfy the perturbation equations for the unstrained vortex,

$$\left(\omega\mathcal{L} - k\mathcal{P} + \mathrm{i}\mathcal{M}(m) - \frac{\mathrm{i}}{Re}\mathcal{V}(m, k)\right)\tilde{\boldsymbol{u}} = 0, \tag{4.3}$$

where $\mathcal{M}(m)$ and $\mathcal{V}(m, k)$ are obtained by replacing $\partial/\partial\theta$ with im and $\partial/\partial z$ with ik, in the matrix operators $\mathcal{M}$ and $\mathcal{V}$, given in Appendix A.

To identify the possible coupling of two Kelvin modes with the strain field, one should identify two neutral Kelvin modes (ω_A, k_A, m_A) and (ω_B, k_B, m_B) that satisfy

$$\omega_A = \omega_B, \qquad k_A = k_B, \qquad m_B - m_A = 3. \tag{4.4}$$

In the presence of viscosity, these modes are always damped, i.e. $\mathrm{Im}(\omega) < 0$. While some modes become neutral as the Reynolds number tends to infinity, others remain damped due to the presence of a critical layer (Sipp & Jacquin 2003).

5. Kelvin modes of the Batchelor vortex

5.1. *Numerical computation of the Kelvin modes*

The Kelvin modes of the unstrained Batchelor vortex are computed by numerically solving the set of (4.3), along with the appropriate boundary conditions, which together form an eigenvalue problem. At $r = \infty$, all the eigenfunctions u, v, w and p must decay exponentially to zero for $k \neq 0$ (the case $k = 0$ is not considered). At the vortex centre, $r = 0$, a regular singularity is encountered, and the asymptotic forms of the eigenfunctions can be derived as

$$\tilde{u} = O(r), \qquad \tilde{v} = O(r), \qquad \tilde{w} = O(1), \qquad \tilde{p} = O(1), \tag{5.1}$$

for $m = 0$, and

$$\tilde{u} = O\left(r^{|m|-1}\right), \qquad \tilde{v} = O\left(r^{|m|-1}\right), \qquad \tilde{w} = O\left(r^{|m|}\right), \qquad \tilde{p} = O\left(r^{|m|}\right), \tag{5.2}$$

for $|m| \neq 0$. The numerical approach to solve this eigenvalue problem closely follows the method used in AHL25, with the only difference being the inclusion of a small axial flow in the present study. A Chebyshev spectral collocation method is employed, following the procedure outlined by Fabre & Jacquin (2004). The original domain $0 < r < \infty$ is extended symmetrically to $-\infty < r < \infty$ and mapped onto a contour in the complex-r plane. The problem is then discretised in the Chebyshev domain $(-1, 1)$ using $2(N + 1)$ collocation points, where a resolution of $N = 200$ is found to be sufficient. In the inviscid case, we apply a complex mapping similar to that used by Fabre & Jacquin (2004), defined by

$$r = \frac{H\xi}{1 - \xi^2} + \mathrm{i}\frac{A\xi}{\sqrt{1 - \xi^2}}, \tag{5.3}$$

where H controls the radial distribution of the collocation points and A sets the tilt of the contour into the complex plane. We also exploit the parity properties of the eigenfunctions to optimise the computation. For odd azimuthal wavenumbers m, $\tilde{w}$ and $\tilde{p}$ are expanded in

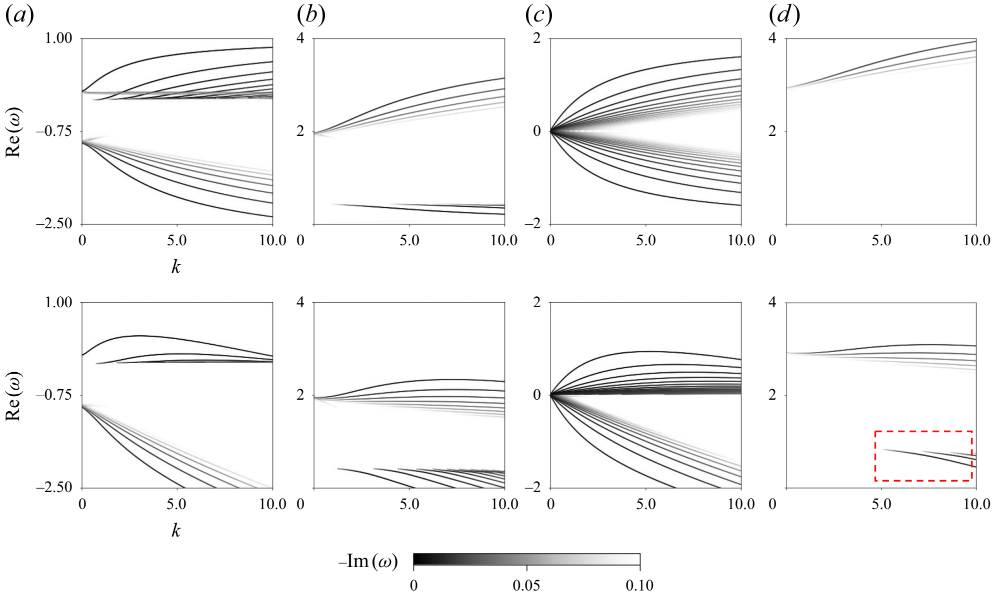

Figure 3. Effects of axial flow on the dispersion curves (Re(ω) vs k) of Kelvin modes of the Batchelor vortex, computed at $\mathrm{Re}=10^4$ by integration along the real axis. Each point represents a mode, with its greyscale intensity corresponding to the damping rate $-\mathrm{Im}(\omega)$: darker points indicate lower damping ($=0$) and lighter points higher damping ($=0.1$). Top panels show results for $W_0=0$ (Lamb–Oseen vortex) and bottom panels for $W_0=-0.1$. Results are shown for (*a*) $m=-1$, (*b*) $m=2$, (*c*) $m=0$ and (*d*) $m=3$.

odd polynomials, while $\tilde{u}$ and $\tilde{v}$ use even polynomials. For even m, the roles are reversed, with $\tilde{w}$ and $\tilde{p}$ using even polynomials and $\tilde{u}$ and $\tilde{v}$ using odd polynomials.

The effect of axial flow on the dispersion curves is illustrated in figure 3 for $m=-1$, 0, 2 and 3. Throughout this paper, we focus on negative values of W_0, ensuring that the axial wavenumber k remains positive and the signs of m and Re(ω) are preserved. As shown in the figure, increasing the magnitude of W_0 causes the dispersion curves to shift downward. For $m=0$, the curves, which are symmetric about zero when $W_0=0$, lose their symmetry once axial flow is introduced. Another notable effect is observed for $m=3$: at $W_0=-0.1$, new branches (highlighted by the red dashed rectangle) emerge that were previously suppressed by the critical layer when $W_0=0$. The appearance of these modes enables new resonance possibilities with $m=0$ modes, potentially leading to triangular instability. Similarly, this happens for other azimuthal pairs such as (1, 4), (2, 5) and beyond. The nature of these modes will be discussed in the next section.

Figure 4 illustrates the effect of axial flow on the crossing points of the dispersion curves for $m=-1$ and $m=2$. Before proceeding with the discussion, we first establish the notation that will be used throughout the paper to refer to modes constituting a resonant azimuthal wavenumber pair (m_A, m_B). For example, the results shown in the figure correspond to the pair $(m_A, m_B)=(-1, 2)$, where $m_A=-1$ and $m_B=2$. The labels $[l_A, l_B]$ denote the respective branches of the dispersion curves to which the modes of m_A and m_B belong. For instance, $[l_A, l_B]=[1, 2]$ indicates that the mode associated with m_A lies on its first branch, while the mode for m_B lies on its second branch. For brevity, we will sometimes use the notation $(m_A, m_B, [l_A, l_B])$ to refer to both the azimuthal wavenumbers of a resonant pair and their associated branches.

From figure 4, it is evident that at $W_0=0$, some branches of $m=2$ were heavily damped by the critical layer and could not form crossing points with $m=-1$. However, at

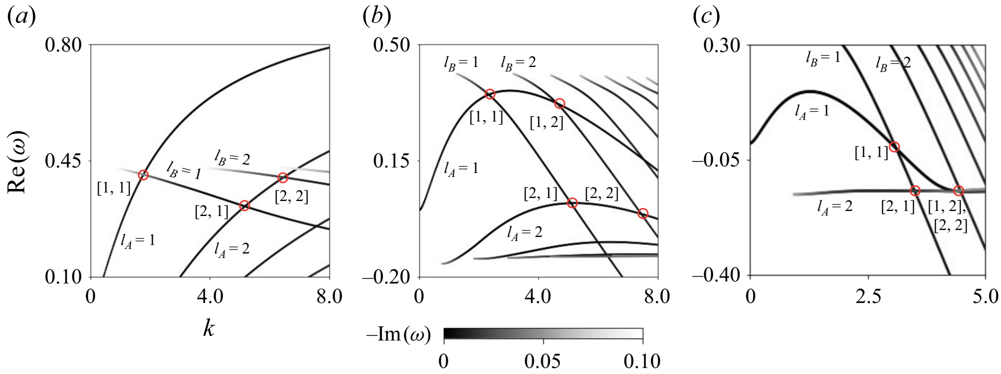

Figure 4. Effects of axial flow on the crossing points of the dispersion curves (Re(ω) vs k) for $m_A = -1$ and $m_B = 2$. Results are shown for (*a*) $W_0 = 0$, (*b*) $W_0 = -0.1$ and (*c*) $W_0 = -0.3$. Each point represents a mode, with its greyscale intensity corresponding to the damping rate $-\mathrm{Im}(\omega)$: darker points indicate lower damping ($= 0$) and lighter points higher damping ($= 0.1$).

$W_0 = -0.1$, these modes become less damped and are able to form crossing points. For instance, the resonant pair [1, 2] does not exist at $W_0 = 0$ but appears at $W_0 = -0.1$. Additionally, the critical-layer damping associated with the pairs [1, 1] and [2, 2] can be seen to weaken as W_0 decreases from 0 to -0.1.

Another important observation is that the resonant modes originating from $m = -1$, which were undamped at $W_0 = 0$, can become damped at higher magnitudes of axial flow for specific values of k and W_0. For example, at $W_0 = -0.3$, the modes corresponding to the pairs [2, 1] and [2, 2] are significantly damped by the critical layer.

While these observations are qualitative, based on visual inspection of the dispersion curves, they clearly illustrate how axial flow alters the characteristics of resonant modes. A more detailed and quantitative classification of these effects will be provided in the next section.

5.2. *Large-k asymptotic prediction of the Kelvin modes*

In this section we discuss the asymptotic nature of the various kinds of modes that can exist for the Batchelor vortex in the inviscid limit. Le Dizès & Lacaze (2005) developed an asymptotic framework based on WKB analysis to characterise the different types of Kelvin modes that arise in the limits of infinite Reynolds numbers and large axial wavenumbers. The essential characteristics of these modes can be determined by examining three functions: the epicyclic frequencies $\omega^{\pm}(r)$ and the critical frequency $\omega_c(r)$, defined as

$$\omega^{\pm}(r) = m\Omega_0(r) + k\overline{W}_0 \pm \sqrt{2\Omega_0(r)\zeta_0(r)}, \tag{5.4}$$

$$\omega_c(r) = m\Omega_0(r) + k\overline{W}_0, \tag{5.5}$$

where $\overline{W}_0$ is given in (3.8), and $\Omega_0(r)$ and $\zeta_0(r)$ are defined in § 3.2.

For given values of m, k and W_0, these functions can be plotted to identify the frequency ranges corresponding to different mode types: (i) regular or singular neutral modes, and (ii) core or ring modes. In the case of the Lamb–Oseen vortex ($W_0 = 0$), the curves are independent of k, resulting in identical profiles for all axial wavenumbers. However, for the Batchelor vortex, each value of k yields distinct $\omega^{\pm}(r)$ and $\omega_c(r)$ profiles, leading to a unique frequency range for each mode type.

Figure 5 shows plots of $\omega^{\pm}(r)$ and $\omega_c(r)$ for $m = 2$ in two cases, $kW_0 = 0$ and $kW_0 = -4$, illustrating the domains where each type of mode can exist. To determine the nature

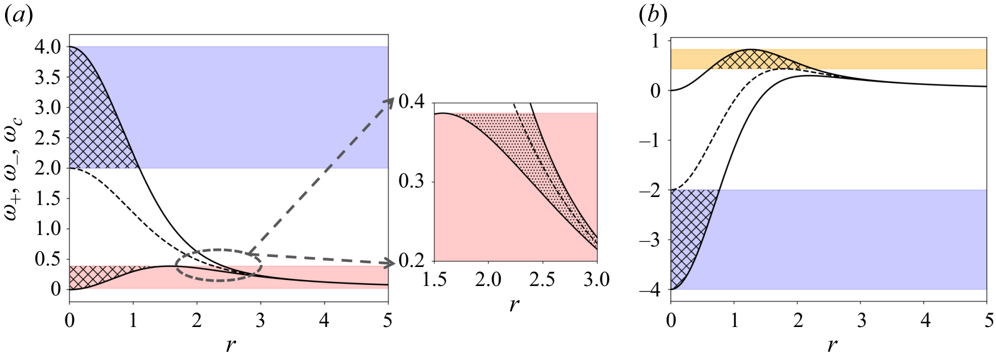

Figure 5. Plots of the epicyclic frequencies ω^+ and ω^- (solid lines) and the critical frequency ω_c (dashed line) as functions of the radial coordinate r. Results are shown for (*a*) $m = 2$, $kW_0 = 0$, with an inset showing a zoomed-in view of the indicated region; (*b*) $m = 2$, $kW_0 = -4$. The blue and red shaded areas represent the domains of regular neutral core modes and singular neutral core modes, respectively. In (*b*) the yellow shaded region corresponds to regular ring modes. Hatched regions denote the regions where modes are localised. The dotted region in the inset of (*a*) highlights where singular neutral modes encounter a critical point given by ω_c.

of a mode with a given frequency, one can draw a horizontal line at that frequency value. The region enclosed between the curves $\omega^{\pm}(r)$ is where the modes are localised and have oscillatory behaviour, and decay exponentially to zero in the areas outside this region. The intersection points with the $\omega^{\pm}(r)$ curves are the WKB turning points. Intersections with the $\omega_c(r)$ curve mark critical point singularities in r. Based on the locations of these intersection points, the type of mode can be classified as follows.

5.2.1. *Regular neutral modes vs singular neutral modes*

A mode is classified as a regular neutral mode if it does not encounter any critical point singularities in r – that is, if a horizontal line drawn at its frequency does not intersect $\omega_c(r)$ anywhere. In figure 5, regions where modes are regular are shaded in blue. However, if a mode encounters a critical point at large r – after passing through at least two turning points, as indicated by the red regions in the figure – it is classified as a singular neutral mode and undergoes asymptotically small critical-layer damping. Such modes are often referred to as critical-layer waves. When solving (4.3), the critical point can be avoided by deforming the integration contour into the complex plane, either above or below the critical point, depending on its trajectory in the complex plane (Le Dizès 2004). Alternatively, the critical point can be regularised by introducing viscosity while remaining on the real axis. As a result, the structure of such modes is divided into two distinct radial regions: in the first region, the mode is oscillatory like a regular neutral mode, while in the second region (illustrated by the zoomed inset in figure 5*a*), the mode exhibits additional oscillations induced by the regularisation of the critical layer. The additional modes that appeared for $m = 3$ in the presence of axial flow, seen in figure 3(*d*), are singular neutral modes. Singular neutral modes exist for all $m \neq 0$ in specific frequency ranges.

It is also insightful to compare the structures of a regular neutral mode with those of a singular neutral mode. Figure 6 illustrates this by showing the axial vorticity fields of one representative regular neutral mode from the blue region and one singular neutral mode from the red region in figure 5(*a*). In the latter, additional oscillations caused by the critical-layer regularisation can be observed in figure 6(*c*). The 2-D structure of the singular neutral mode, shown in figure 6(*b*), is also characterised by spiral arms in the critical layer, while retaining a regular wave structure in the inner region similar to that of the regular neutral mode displayed in figure 6(*a*).

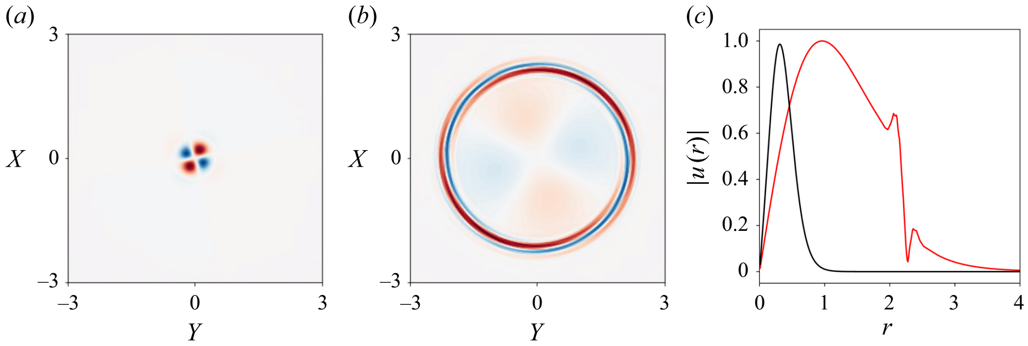

Figure 6. Comparison of the structures of a regular neutral mode and a singular neutral mode obtained at $\mathrm{Re} = 10^4$, $m = 2$, $kW_0 = 0$. (*a*) Regular neutral mode: 2-D contours of axial disturbance vorticity for the mode with $k = 10.0$, $\mathrm{Re}(\omega) = 3.138$, $\mathrm{Im}(\omega) = -0.020$; (*b*) singular neutral mode: $k = 1.76$, $\mathrm{Re}(\omega) = 0.407$, $\mathrm{Im}(\omega) = -0.045$; (*c*) radial distribution of the absolute value of the eigenfunction $|u(r)|$, with the black curve corresponding to the mode in (*a*) and the red curve to the mode in (*b*).

If a critical point is encountered before passing through at least two turning points, the mode is completely suppressed by the critical layer in the inviscid limit, although it can still exist as a strongly damped viscous mode at lower Reynolds numbers (Fabre *et al.* 2006). The unshaded regions in figure 5 correspond to the domains where such modes exist.

5.2.2. *Core modes versus ring modes*

Based on the radial location where the modes are localised, they can be classified as either core modes or ring modes. A mode is termed a core mode if the vortex centre ($r = 0$) lies within the region where the mode is localised – that is, the mode is confined between the centre and a turning point defined by either of the curves $\omega^{\pm}(r)$. All the modes in the blue and red shaded regions of figures 5(*a*) and 5(*b*) fall into this category. In contrast, a ring mode is localised away from the vortex centre and lies between two turning points given by $\omega^{\pm}(r)$. The yellow shaded region in figure 5(*b*) shows such modes. In general, core modes in a Batchelor vortex are expected for frequencies satisfying $-2 < \omega - m - kW_0 < 2$, whereas ring modes appear outside this range.

Figure 7 compares the structures of a core mode and a ring mode, selected respectively from the blue and yellow regions of figure 5(*b*). For the ring mode, the region where it is localised is shifted to larger values of r, in contrast to the core mode, where it is localised close to the centre. The hollow centre and annular structure characteristic of a ring mode are also clearly visible in its 2-D profile.

5.2.3. *Predicted resonance domain of triangular instability*

In AHL25 we demonstrated that for the Lamb–Oseen vortex, the $m = 2$ (or -2) modes in the resonant pairs correspond to singular neutral core modes, while the $m = 1$ (or -1) modes are regular neutral core modes. In contrast, for the Batchelor vortex, as mentioned before, each value of k yields distinct epicyclic and critical frequency profiles, allowing for resonant combinations involving a wider range of mode types, including ring modes. By using the expressions for $\omega^{\pm}(r)$ and $\omega_c(r)$ in (5.4) and (5.5), along with the triangular instability resonance condition given in (4.4), we analysed all possible resonant azimuthal wavenumber pairs within the $(\mathrm{Re}(\omega), kW_0)$ parameter space. The resulting resonance domains are shown in figure 8 for the pairs $(m_A, m_B) = (-1, 2)$, $(0, 3)$ and $(1, 4)$. The results can be summarised as follows.

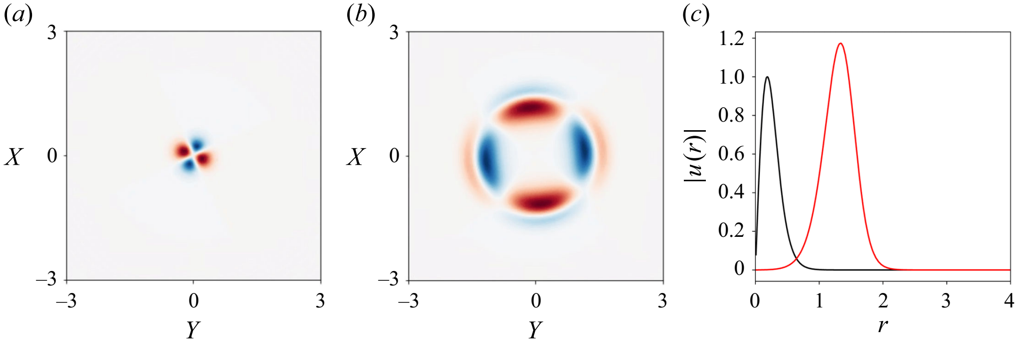

Figure 7. Comparison of the structures of a regular core mode and a regular ring mode, obtained at $\mathrm{Re} = 10^4$, $m = 2$, $kW_0 = -4$. (a) Core mode: 2-D contours of axial disturbance vorticity for the mode with $k = 10.0$, $\mathrm{Re}(\omega) = -3.252$, $\mathrm{Im}(\omega) = -0.016$; ($b$) ring mode: $k = 10.0$, $\mathrm{Re}(\omega) = 0.719$, $\mathrm{Im}(\omega) = -0.011$; ($c$) radial distribution of the absolute value of the eigenfunction $|u(r)|$, with the black curve corresponding to the mode in (a) and the red curve to the mode in (b).

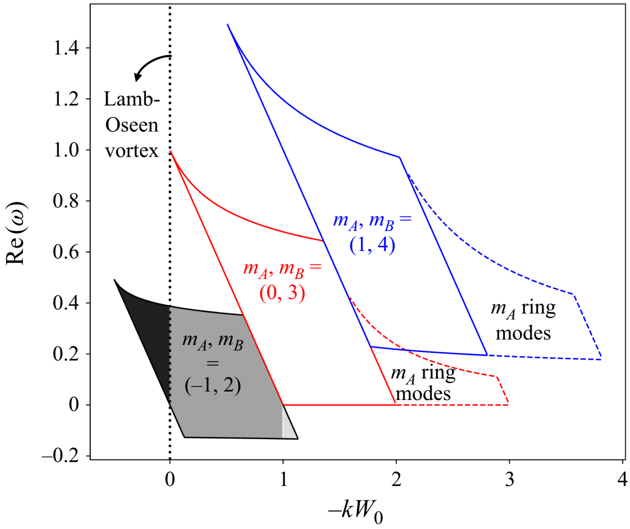

Figure 8. Domain of possible resonance between Kelvin modes of the Batchelor vortex, shown for the azimuthal wavenumber pairs $(m_A, m_B) = (-1, 2)$, $(0, 3)$ and $(1, 4)$, indicated in black, red and blue, respectively. Solid lines represent resonance domains involving core modes, while dashed lines correspond to ring modes of m_A. In the $(-1, 2)$ domain, the black shaded region indicates resonances involving singular modes of $m = 2$ only; the mid-grey region corresponds to resonances involving singular modes of both $m = -1$ and $m = 2$; and the pale grey region corresponds to resonances involving singular modes of $m = -1$ only. The black dotted line at $kW_0 = 0$ represents the Lamb–Oseen vortex case.

(a) For the pair $(-1, 2)$, the nature of the resonant modes depends on the value of kW_0 and can be categorised into the following three regions.

(i) For $kW_0 \geqslant 0$: the m_A modes are regular neutral core modes, while the m_B modes are singular neutral core modes.
(ii) For $-1 < kW_0 < 0$: both m_A and m_B modes are singular neutral core modes.
(iii) For $kW_0 \leqslant -1$: the m_A modes are singular neutral core modes, while the m_B modes are regular neutral core modes.

(*b*) For all higher azimuthal wavenumber pairs such as (0, 3), (1, 4), (2, 5), etc., the nature of the modes are as follows.

(i) The modes corresponding to m_A are always regular neutral core modes or ring modes.
(ii) The modes corresponding to m_B are always singular neutral core modes.

6. Triangular instability characteristics

In the previous section we identified the domains in which resonant Kelvin modes may occur and potentially become unstable through triangular instability, and we used asymptotic analysis to characterise the nature of the modes involved in each resonance. Building on that foundation, this section presents the actual evidence of unstable modes and describes their properties in detail. In § 6.1 we derive the theoretical expression used to compute the growth rate of a resonant pair of Kelvin modes. We then compare, in § 6.2, the growth rates and structural characteristics of the unstable modes obtained from DNS with those predicted by theory using this expression. Once the agreement between DNS and theory is established, we use the predictive power of the theoretical framework to examine in § 6.3 how the characteristics of the unstable modes evolve continuously as the axial flow is varied. Such a parametric study would be prohibitively expensive using DNS alone, making the theoretical approach particularly useful.

6.1. *Theoretical expression for the triangular instability growth rate*

The method for calculating the growth rate linked to the resonant coupling between two Kelvin modes and the triangular strain field follows an asymptotic multiscale analysis in the limit of small ϵ, similar to the approach of Moore & Saffman (1975). The perturbation is modelled as a combination of two normal modes with azimuthal wavenumbers m_A and m_B (related through (4.4)), forming a resonant pair of Kelvin modes at leading order in ϵ. We express the disturbance as

$$\boldsymbol{u} \sim \left(A\tilde{\boldsymbol{u}}_A(r)\mathrm{e}^{\mathrm{i}(m_A\theta)} + B\tilde{\boldsymbol{u}}_B(r)\mathrm{e}^{\mathrm{i}(m_B\theta)} \right) \mathrm{e}^{\mathrm{i}(kz-\omega t)}, \tag{6.1}$$

where the (real) axial wavenumber k and the (complex) frequency ω of both modes are assumed to lie near a resonant point defined by k_c and a real frequency ω_c.

Substituting (6.1) into (4.1) yields two equations corresponding to the components proportional to $\mathrm{e}^{\mathrm{i}m_A\theta}$ and $\mathrm{e}^{\mathrm{i}m_B\theta}$, respectively, i.e.

$$A\left(\omega\mathcal{L} - k\mathcal{P} + \mathrm{i}\mathcal{M}(m_A) - \frac{\mathrm{i}}{Re}\mathcal{V}(m_A, k) \right) \tilde{\boldsymbol{u}}_A = \mathrm{i}B\epsilon\overline{\mathcal{N}}(m_B)\tilde{\boldsymbol{u}}_B, \tag{6.2}$$

$$B\left(\omega\mathcal{L} - k\mathcal{P} + \mathrm{i}\mathcal{M}(m_B) - \frac{\mathrm{i}}{Re}\mathcal{V}(m_B, k) \right) \tilde{\boldsymbol{u}}_B = \mathrm{i}A\epsilon\mathcal{N}(m_A)\tilde{\boldsymbol{u}}_A, \tag{6.3}$$

where $\overline{\mathcal{N}}(m_B)$ and $\mathcal{N}(m_A)$ are obtained by substituting $\partial/\partial\theta$ with $\mathrm{i}m_B$ and $\mathrm{i}m_A$, respectively, in the $\mathcal{N}$ and $\overline{\mathcal{N}}$ operators defined in Appendix A. These coupled equations illustrate how the two modes interact via the straining field, represented by the right-hand side terms.

The complex frequency ω is determined by applying an orthogonality condition using the adjoint resonant Kelvin modes. The adjoint eigenfunctions $\tilde{\boldsymbol{u}}_A^\dagger$ and $\tilde{\boldsymbol{u}}_B^\dagger$ are solutions of the adjoint form of (4.3) for $(m, k) = (m_A, k_c)$ and (m_B, k_c), respectively, defined with respect to the scalar product

$$\langle \boldsymbol{u_1}, \boldsymbol{u_2} \rangle = \int_0^\infty \boldsymbol{u_1^*}(r)\boldsymbol{u_2}(r)\, r\, \mathrm{d}r, \tag{6.4}$$

where '$*$' denotes complex conjugation. We denote the inviscid forms of the Kelvin modes as $(\tilde{\boldsymbol{u}}_A^{(\infty)}, \tilde{\boldsymbol{u}}_B^{(\infty)})$ and their adjoints as $(\tilde{\boldsymbol{u}}_A^{\dagger(\infty)}, \tilde{\boldsymbol{u}}_B^{\dagger(\infty)})$. By taking the scalar product of (6.2) with $\tilde{\boldsymbol{u}}_A^{\dagger(\infty)}$ and of (6.3) with $\tilde{\boldsymbol{u}}_B^{\dagger(\infty)}$, we obtain

$$\left(\omega - \omega_A^{(\infty)} - Q_A^{(\infty)}(k - k_c^{(\infty)}) - \mathrm{i}\frac{V_A^{(\infty)}}{Re}\right) A = \mathrm{i}\epsilon C_{AB}^{(\infty)} B, \tag{6.5}$$

$$\left(\omega - \omega_B^{(\infty)} - Q_B^{(\infty)}(k - k_c^{(\infty)}) - \mathrm{i}\frac{V_B^{(\infty)}}{Re}\right) B = \mathrm{i}\epsilon C_{BA}^{(\infty)} A, \tag{6.6}$$

where the coefficients $Q_A^{(\infty)}$, $Q_B^{(\infty)}$, $V_A^{(\infty)}$, $V_B^{(\infty)}$, $C_{AB}^{(\infty)}$, $C_{BA}^{(\infty)}$ are given by

$$Q_A^{(\infty)} = \frac{\left\langle \tilde{\boldsymbol{u}}_A^{\dagger(\infty)}, \mathcal{P}\tilde{\boldsymbol{u}}_A^{(\infty)} \right\rangle}{\left\langle \tilde{\boldsymbol{u}}_A^{\dagger(\infty)} \mathcal{L}\tilde{\boldsymbol{u}}_A^{(\infty)} \right\rangle}, \quad Q_B^{(\infty)} = \frac{\left\langle \tilde{\boldsymbol{u}}_B^{\dagger(\infty)}, \mathcal{P}\tilde{\boldsymbol{u}}_B^{(\infty)} \right\rangle}{\left\langle \tilde{\boldsymbol{u}}_B^{\dagger(\infty)}, \mathcal{L}\tilde{\boldsymbol{u}}_B^{(\infty)} \right\rangle}, \tag{6.7}$$

$$V_A^{(\infty)} = \frac{\left\langle \tilde{\boldsymbol{u}}_A^{\dagger(\infty)}, \mathcal{V}\tilde{\boldsymbol{u}}_A^{(\infty)} \right\rangle}{\left\langle \tilde{\boldsymbol{u}}_A^{\dagger(\infty)}, \mathcal{L}\tilde{\boldsymbol{u}}_A^{(\infty)} \right\rangle}, \quad V_B^{(\infty)} = \frac{\left\langle \tilde{\boldsymbol{u}}_B^{\dagger(\infty)}, \mathcal{V}\tilde{\boldsymbol{u}}_B^{(\infty)} \right\rangle}{\left\langle \tilde{\boldsymbol{u}}_B^{\dagger(\infty)}, \mathcal{L}\tilde{\boldsymbol{u}}_B^{(\infty)} \right\rangle}, \tag{6.8}$$

$$C_{AB}^{(\infty)} = \frac{\left\langle \tilde{\boldsymbol{u}}_A^{\dagger}, \overline{\mathcal{N}}(m_B)\tilde{\boldsymbol{u}}_B^{(\infty)} \right\rangle}{\left\langle \tilde{\boldsymbol{u}}_A^{\dagger(\infty)}, \mathcal{L}\tilde{\boldsymbol{u}}_A^{(\infty)} \right\rangle}, \quad C_{BA}^{(\infty)} = \frac{\left\langle \tilde{\boldsymbol{u}}_B^{\dagger(\infty)}, \mathcal{N}(m_A)\tilde{\boldsymbol{u}}_A^{(\infty)} \right\rangle}{\left\langle \tilde{\boldsymbol{u}}_B^{\dagger(\infty)}, \mathcal{L}\tilde{\boldsymbol{u}}_B^{(\infty)} \right\rangle}. \tag{6.9}$$

The frequencies $\omega_A^{(\infty)}$ and $\omega_B^{(\infty)}$ represent the inviscid estimates of the resonant Kelvin mode frequencies at $k = k_c^{(\infty)}$. They can be written as

$$\omega_A^{(\infty)} = \omega_c^{(\infty)} + \mathrm{i}\mathrm{Im}\left(\omega_A^{(\infty)}\right), \quad \omega_B^{(\infty)} = \omega_c^{(\infty)} + \mathrm{i}\mathrm{Im}\left(\omega_B^{(\infty)}\right), \tag{6.10}$$

where $\mathrm{Im}(\omega_A^{(\infty)})$ and $\mathrm{Im}(\omega_B^{(\infty)})$ are the critical-layer damping rates of the respective modes.

Equations (6.5)–-(6.6) with (6.10) give a quadratic equation for the complex frequency ω as a function of k, i.e.

$$\left(\omega - \omega_A^{(\infty)} - Q_A^{(\infty)}(k - k_c^{(\infty)}) - \mathrm{i}\frac{V_A^{(\infty)}}{Re}\right)\left(\omega - \omega_B^{(\infty)} - Q_B^{(\infty)}(k - k_c^{(\infty)}) - \mathrm{i}\frac{V_B^{(\infty)}}{Re}\right) = -\epsilon^2 (N^{(\infty)})^2, \tag{6.11}$$

where

$$N^{(\infty)} = \sqrt{C_{AB}^{(\infty)} C_{BA}^{(\infty)}}. \tag{6.12}$$

The growth rate σ is defined as $\mathrm{Im}(\omega)$, and a growth rate band around the resonant axial wavenumber $k_c^{(\infty)}$ can be computed using the equations above. Both modes oscillate with a common resonant frequency given by $\mathrm{Re}(\omega)$. The right-hand side represents the coupling term driving the instability. The terms $\mathrm{i}V_A^{(\infty)}/\mathrm{Re}$ and $\mathrm{i}V_B^{(\infty)}/\mathrm{Re}$ are volumic viscous damping terms and vanish when computing the inviscid growth rate. The following equations

$$\omega - \omega_A^{(\infty)} - Q_A^{(\infty)}(k - k_c^{(\infty)}) = 0, \tag{6.13}$$

$$\omega - \omega_B^{(\infty)} - Q_B^{(\infty)}(k - k_c^{(\infty)}) = 0, \tag{6.14}$$

are the linear approximates of the inviscid dispersion relations for the respective azimuthal wavenumbers of the unstrained vortex. These provide the value of ω for modes with $k = k_c^{(\infty)} + \tau$ near the resonant point and are expected to closely approximate the original dispersion relations for small τ up to $O(10^{-1})$. In particular, the linear approximation of the variation of critical-layer damping values with k can therefore be expressed as

$$\omega_{\mathrm{CL},A}^{(\infty)} = \mathrm{Im}(\omega_A^{(\infty)}) + \mathrm{Im}(Q_A^{(\infty)})\tau, \tag{6.15}$$

$$\omega_{\mathrm{CL},B}^{(\infty)} = \mathrm{Im}(\omega_B^{(\infty)}) + \mathrm{Im}(Q_B^{(\infty)})\tau, \tag{6.16}$$

respectively, for each mode. If τ becomes too large, the linear approximation breaks down and the predicted critical-layer damping may incorrectly become positive, which is nonphysical. While this could, in principle, be corrected by retaining higher-order terms in τ, such refinements lie beyond the scope of the present analysis. Instead, for all $k = k_c^{(\infty)} + \tau$, any positive values of critical-layer damping obtained from (6.15) and (6.16) are set to zero when computing the growth rate. This adjustment does not affect the behaviour at the resonant point k_c and is required only for values of k sufficiently far from k_c where the linear approximation ceases to be valid. This procedure is applied consistently throughout the following two sections.

6.2. *Unstable modes: numerical results and theoretical predictions*

For any resonant pair of Kelvin modes with azimuthal wavenumbers m_A and m_B, the theoretical growth rate can be evaluated using (6.11). We can thus compare and validate the unstable modes identified numerically through DNS against the predictions of the theoretical framework. To this end, three sets of linearised Navier–Stokes simulations were performed using base flows corresponding to $W_0 = -0.1$, -0.2 and -0.3 at $\mathrm{Re} = 10^4$ and remind the reader that $\epsilon = 0.008$ for these base flows. These particular values of W_0 were chosen simply because they are small enough to ensure that no inviscid or viscous centre modes of the unstrained Batchelor vortex become unstable, as discussed in the introduction. They also provide a sufficiently broad range of unstable modes to allow meaningful comparison and interpretation. The choice $\mathrm{Re} = 10^4$ is large enough for non-viscous approximations to be meaningful and sufficiently large for the unstable modes to not be completely suppressed by viscous damping, while also still keeping the DNS computationally tractable. From a practical point of view, although typical wind-turbine Reynolds numbers are much higher, we argue that our study is particularly relevant for laboratory-scale experiments where Re is in the range 10^3–10^4.

Starting from a random initial energy distribution, unstable modes with various azimuthal wavenumbers grow exponentially in time. Their growth rate is obtained as half the slope of the logarithmic time evolution of the mode's energy, while the mode frequency is determined by tracking the phase of the disturbance and measuring its angular rotation rate about the z axis.

For ease of reference, the resonant modes obtained at $W_0 = -0.1$ are labelled A1, A2, etc.; those at $W_0 = -0.2$ as B1, B2, etc.; and those at $W_0 = -0.3$ as C1, C2, etc. For each of these three values of W_0, we present both the dispersion and growth rate curves of the resonant modes, together with their 2-D structures obtained from DNS. For $W_0 = -0.1$, figure 9 shows, in the top panels, the dispersion curves of the Kelvin modes obtained by numerically solving the set of (4.3) as discussed in § 5.1, and the corresponding crossing points for each azimuthal wavenumber pair (m_A, m_B). The resonant modes that yield positive growth rates at $\mathrm{Re} = 10^4$ are highlighted with circles. In the bottom panels of the same figure, we plot the corresponding theoretical and DNS growth rate curves σ as

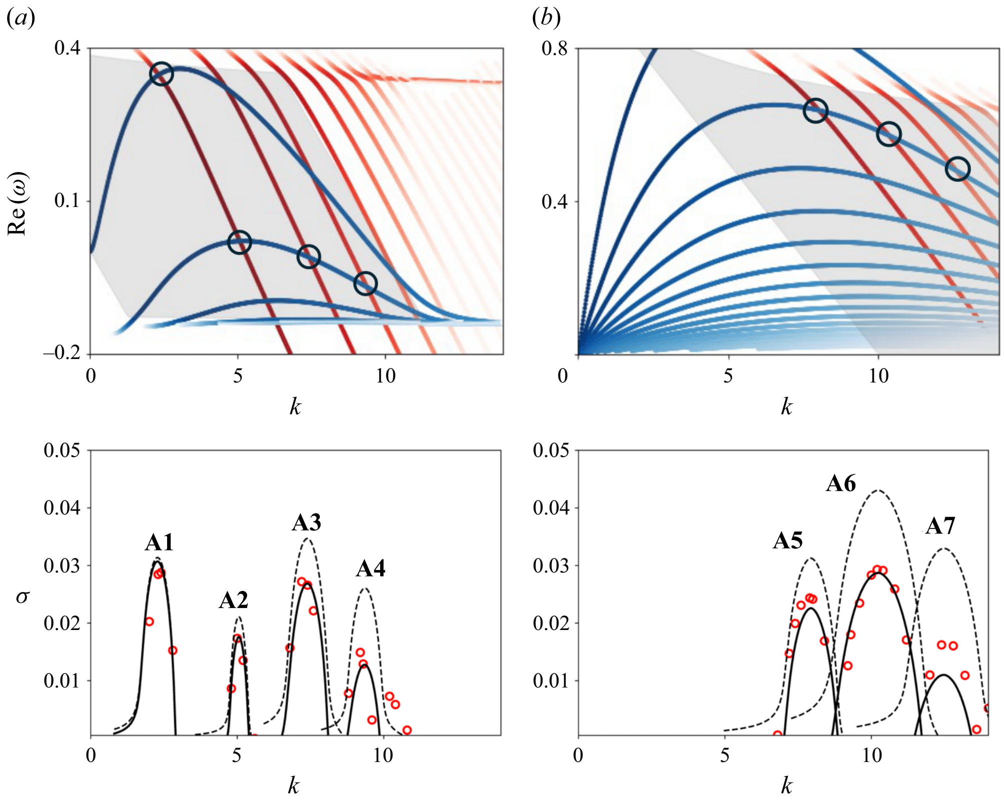

Figure 9. Resonant modes A1, A2, etc. and their growth rates at $W_0 = -0.1$. Top panels: dispersion curves showing $\mathrm{Re}(\omega)$ vs k for (*a*) $(m_A, m_B) = (-1, 2)$ and (*b*) (0, 3). Red curves represent m_B modes, blue curves represent m_A modes, with colour transitions indicating increasing damping (from 0 to −0.05). Resonant modes are marked with black circles at the crossing points. Grey background regions in the top panels mark the core mode resonance domain predicted by the asymptotic theory. Bottom panels: growth rate curves σ vs k; solid black lines show the viscous case ($\mathrm{Re} = 10^4$), dashed lines show the inviscid case and red circles indicate DNS results.

functions of k for the circled modes. These growth rate curves are also compared with the corresponding inviscid growth rate curves predicted by theory. The purpose of comparing with inviscid growth rates is to highlight the maximum growth rate attainable by each mode, which occurs in the inviscid limit. The associated x–y plane structures of these unstable modes, shown as contours of the axial disturbance vorticity field, are presented in figure 10. The periphery of the base hub vortex is indicated in the figure using a dotted circle with radius equal to one for reference. The same organisation is used for $W_0 = -0.2$ in figures 11 and 12, and for $W_0 = -0.3$ in figures 13 and 14. In all cases, only the circled modes in the top panels exhibit positive growth rates at $\mathrm{Re} = 10^4$, as they originate from the first few branches (up to the third, at most) of the dispersion curves. Modes associated with higher branches undergo strong volumic viscous damping and/or weak coupling, leading to negligible growth rates even in the inviscid limit. Consequently, our analysis and comparison focus exclusively on these circled modes, labelled according to the notation described above.

From the bottom panels of figures 9, 11 and 13, we can see that for $W_0 = -0.1$, the mode pairs $(m_A, m_B) = (-1, 2)$ and (0, 3) become resonant and exhibit positive growth rates. At $W_0 = -0.2$, the pairs (−1, 2), (0, 3), (1, 4) and (2, 5) show modes with positive

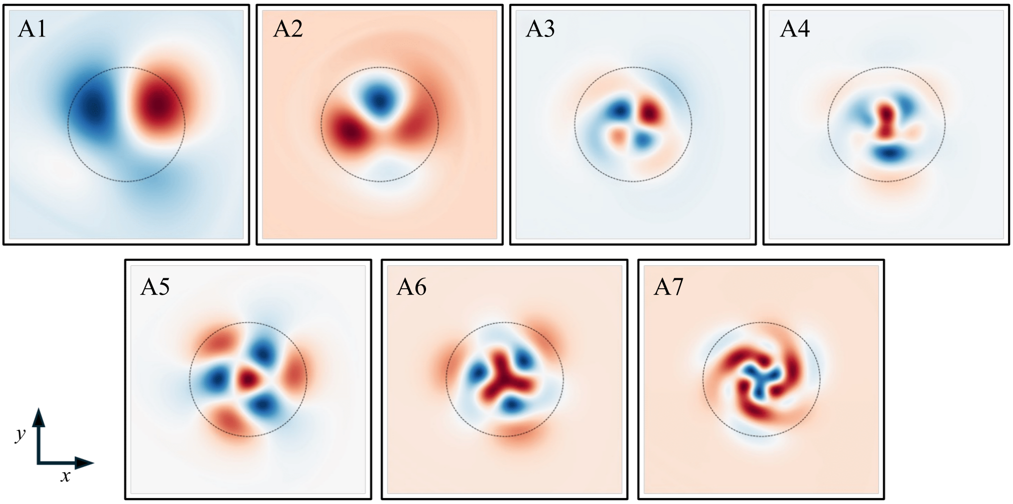

Figure 10. Axial flow strength $W_0 = -0.1$; 2-D structures of the modes labelled A1, A2, etc., obtained from DNS, showing contours of axial vorticity in the x-y plane. Red regions indicate positive vorticity, while blue regions indicate negative vorticity. Domain: $-2 < X, Y < 2$. The hub-vortex boundary is indicated with a dotted circle for reference.

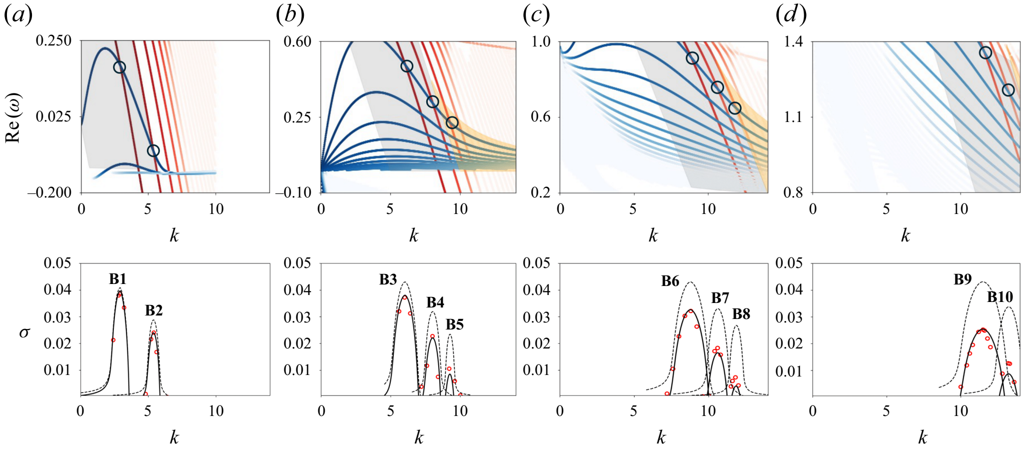

Figure 11. Resonant modes B1, B2, etc. and their growth rates at $W_0 = -0.2$. Top panels: dispersion curves showing $\mathrm{Re}(\omega)$ vs k for (*a*) $(m_A, m_B) = (-1, 2)$, (*b*) $(0, 3)$, (*c*) $(1, 4)$ and (*d*) $(2, 5)$. Red curves represent m_B modes, blue curves represent m_A modes, with colour transitions indicating increasing damping (from 0 to -0.05). Resonant modes are marked with black circles at the crossing points. Grey background regions in the top panels mark the core mode resonance domain predicted by the asymptotic theory, while orange regions represent the resonance domain for ring modes of m_A. Bottom panels: growth rate curves σ vs k; solid black lines show the viscous case ($\mathrm{Re} = 10^4$), dashed lines show the inviscid case and red circles indicate DNS results.

growth rates. At $W_0 = -0.3$, positive growth rates are again obtained for modes from $(-1, 2)$, $(0, 3)$ and $(1, 4)$. Overall, the numerical results and theoretical predictions of the growth rates show good agreement, with only modes A7, B5, B8 and B10 exhibiting slight under-prediction by the theory. Additionally, in the bottom panel of figure 9(*a*), we observe another mode to the right of A4 that shows a positive growth rate in the numerical results, while the theoretical prediction yields zero growth. Upon closer inspection, it appears that unstable modes associated with higher branches tend to exhibit this under-prediction of

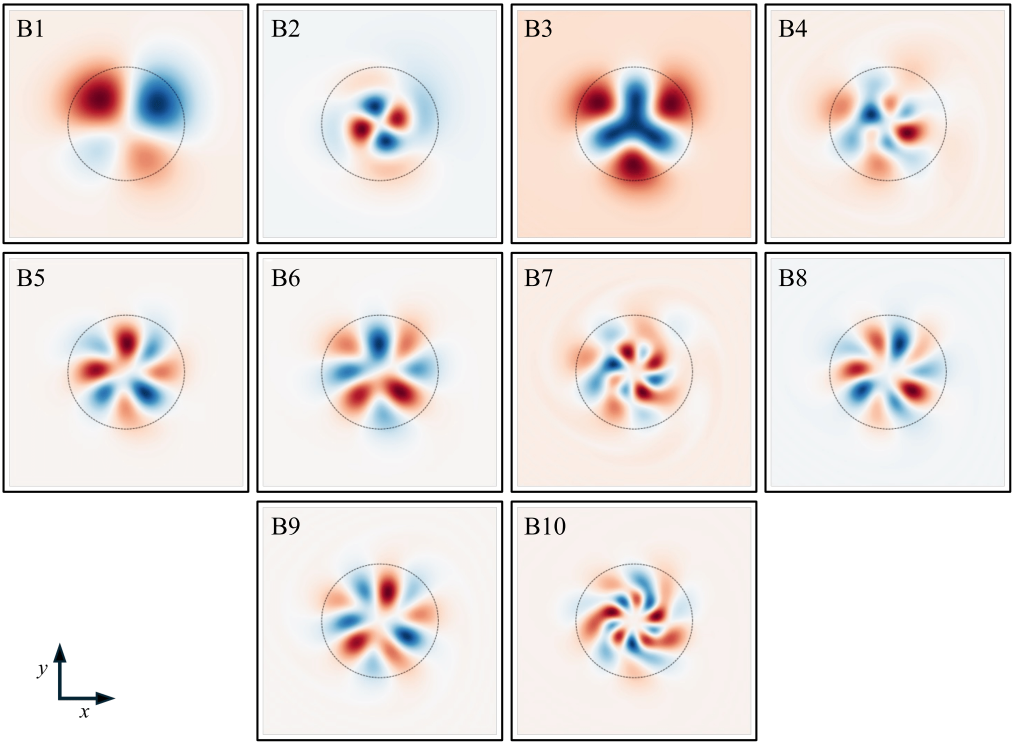

Figure 12. Axial flow strength $W_0 = -0.2$; 2-D structures of the modes labelled B1, B2, etc., obtained from DNS, showing contours of axial vorticity in the x–y plane. Red regions indicate positive vorticity, while blue regions indicate negative vorticity. Domain: $-2 < X, Y < 2$. The hub-vortex boundary is indicated with a dotted circle for reference.

growth rates by the theory. This is most likely due to the over-estimation of the volumic viscous damping in the theoretical model – the coefficients $V_A^{(\infty)}$ and $V_B^{(\infty)}$ – whose magnitudes are generally larger for modes belonging to higher branches (see table 1 in AHL25 for example). As a result, the growth rates of such modes are more sensitive to even small over-predictions of these viscous damping terms, leading to discrepancies between theory and DNS.

Table 1 summarises the composition of all numerically obtained modes for $W_0 = -0.1$, -0.2 and -0.3. For each mode, the table lists the primary azimuthal wavenumber pair $(m_A, m_B, [l_A, l_B])$, any secondary resonant pairs when present and the corresponding energy distribution among different azimuthal wavenumbers m. Note that some of the A, B and C modes share the same $(m_A, m_B, [l_A, l_B])$ composition, with only their characteristics and structures changing as the axial flow varies. For example, A1, B1 and C1 all correspond to $(-1, 2, [1, 1])$; B3 and C2 correspond to $(0, 3, [1, 1])$; A5 and C3 to $(0, 3, [2, 1])$; and B6 and C5 to $(1, 4, [1, 1])$.

It is also worth noting that, upon examining the growth rate curves (and the dispersion curves), some modes appear to be influenced by weak resonances from other modes. In such cases, the axial wavenumber k of the primary resonant pair for a given mode lies within the growth rate band of another mode belonging to a different (m_A, m_B) pair. We refer to these additional contributions as secondary compositions. Table 1 lists only those secondary compositions that contribute a non-negligible amount of energy.

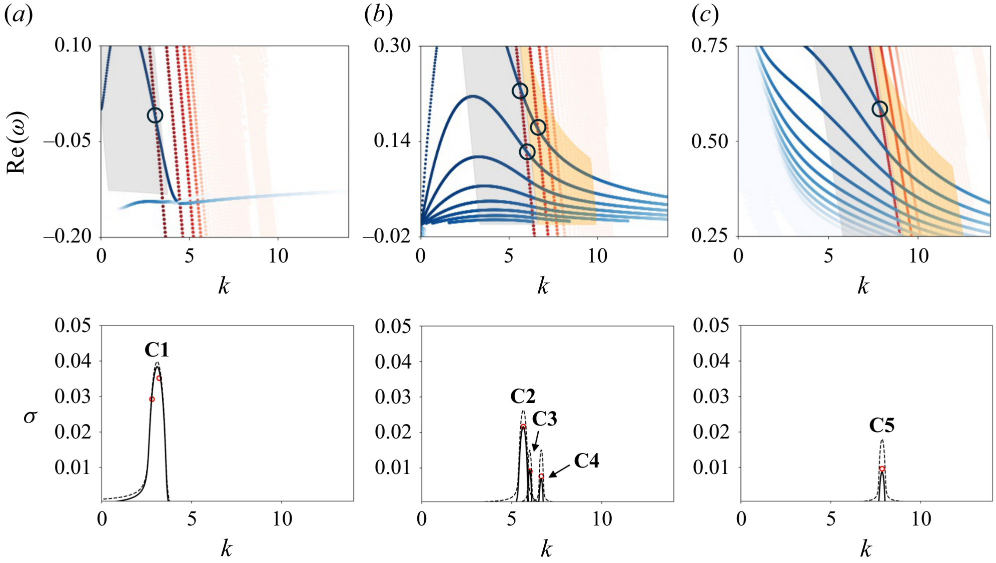

Figure 13. Resonant modes C1, C2, etc. and their growth rates at $W_0 = -0.3$. Top panels: dispersion curves showing Re(ω) vs k for (*a*) $(m_A, m_B) = (-1, 2)$, (*b*) (0, 3) and (*c*) (1, 4). Blue–green curves represent m_B modes, black–brown curves represent m_A modes, with colour transitions indicating increasing damping (from 0 to -0.05). Resonant modes are marked with black circles at the crossing points. Grey background regions in the top panels mark the core mode resonance domain predicted by the asymptotic theory, while orange regions represent the resonance domain for ring modes of m_A. Bottom panels: growth rate curves σ vs k; solid black lines show the viscous case ($\mathrm{Re} = 10^4$), dashed lines show the inviscid case and red circles indicate DNS results.

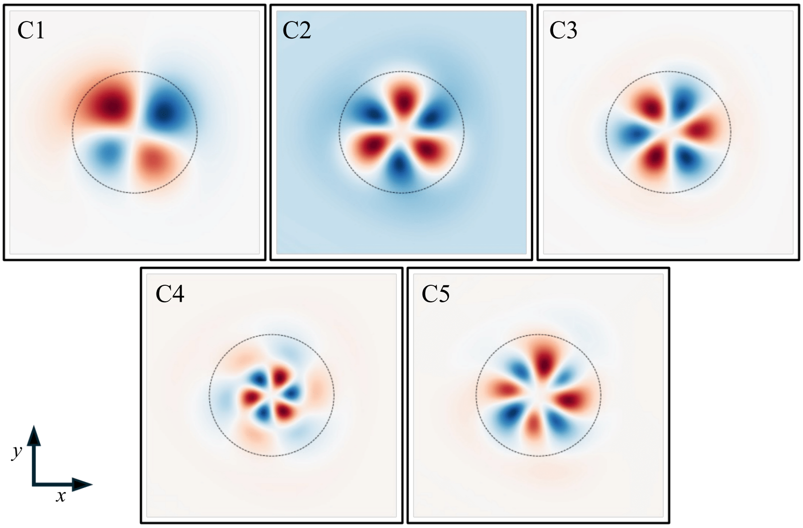

Figure 14. Axial flow strength $W_0 = -0.3$; 2-D structures of the modes labelled C1, C2, etc., obtained from DNS, showing contours of axial vorticity in the x–y plane. Red regions indicate positive vorticity, while blue regions indicate negative vorticity. Domain: $-2 < X, Y < 2$. The hub-vortex boundary is indicated with a dotted circle for reference.

W_0	Mode label	$(m_A, m_B, [l_A, l_B])$ Primary	Secondary	$m = -1$	0	1	2	3	4	5
−0.1	A1	(−1, 2, [1, 1])	—	0.766	0	0	0.233	0	0	0
	A2	(−1, 2, [2, 1])	—	0.403	0.010	0	0.584	0	0	0
	A3	(−1, 2, [2, 2])	—	0.470	0.006	0	0.518	0.005	0	0
	A4	(−1, 2, [2, 3])	A6	0	0.508	0	0	0.491	0	0
	A5	(0, 3, [2, 1])	A3	0.110	0.433	0	0.105	0.351	0	0
	A6	(0, 3, [2, 2])	—	0	0.538	0	0	0.461	0	0
	A7	(0, 3, [2, 3])	—	0	0.551	0	0	0.448	0	0
−0.2	B1	(−1, 2, [1, 1])	—	0.621	0	0	0.379	0	0	0
	B2	(−1, 2, [1, 2])	—	0.560	0	0	0.440	0	0	0
	B3	(0, 3, [1, 1])	—	0	0.545	0	0	0.455	0	0
	B4	(0, 3, [1, 2])	B6	0	0.197	0.371	0	0.175	0.256	0
	B5	(0, 3, [1, 3])	B6	0	0	0.531	0	0	0.468	0
	B6	(1, 4, [1, 1])	—	0	0	0.513	0	0	0.486	0
	B7	(1, 4, [1, 2])	B9	0	0	0.380	0.174	0	0.330	0.114
	B8	(1, 4, [1, 3])	B9	0	0	0	0.535	0	0	0.464
	B9	(2, 5, [1, 1])	—	0	0	0	0.521	0	0	0.478
	B10	(2, 5, [1, 2])	—	0	0	0	0.541	0	0	0.457
−0.3	C1	(−1, 2, [1, 1])	—	0.554	0	0	0.446	0	0	0
	C2	(0, 3, [1, 1])	—	0	0.429	0	0	0.570	0	0
	C3	(0, 3, [2, 1])	—	0.001	0.285	0.017	0.004	0.692	0	0
	C4	(0, 3, [1, 2])	—	0	0.427	0.009	0.002	0.561	0	0
	C5	(1, 4, [1, 1])	—	0	0	0.445	0	0	0.554	0

Table 1. Composition of the numerically obtained modes for $W_0 = -0.1$, -0.2 and -0.3. The second column lists the mode labels (A, B, C) corresponding to the respective W_0 values. The third and fourth columns indicate the primary azimuthal wavenumber pairs (m_A, m_B) and their corresponding branches (l_A, l_B), and any secondary resonant pairs, if present. Columns 5–11 show the energy distribution among different azimuthal wavenumbers m, representing the relative contribution of each m component to the total mode energy.

In some modes, the secondary contribution can be quite significant – sometimes comparable to, or even larger than, that of the primary composition. A clear example is mode A4: although its primary pair is $(-1, 2)$, figure 9 shows that its axial wavenumber lies within the growth rate band of mode A6, associated with $(0, 3)$, and table 1 confirms that most of A4's energy comes from this secondary composition.

Other modes where the secondary composition contributes significantly include A5 (A3), B4 (B6), B5 (B6), B7 (B9) and B8 (B9), with the dominant secondary mode indicated in parentheses. Please note that the axial vorticity structures that are shown in figures 10, 12 and 14, naturally include contributions from all relevant secondary resonant pairs whenever they occur.

In table 2 we list the axial wavenumber k, the frequencies from DNS and theory, the maximum viscous growth rates at $\mathrm{Re} = 10^4$ obtained from both approaches and the corresponding inviscid growth rates, allowing us to quantify the extent of viscous damping exhibited by each mode. Overall, the DNS results show very good agreement with the theoretical predictions. The frequencies are also in reasonably close agreement, though a consistent offset is observed: the theoretical values are systematically lower than those obtained from the DNS. At present, we do not have a clear explanation for this discrepancy.

It is also interesting to note that among the modes presented above, ring modes appear only in the B and C sets. In particular, modes B5 and B8 lie within regions where ring modes associated with m_A are expected, while modes C2, C3, C4 and C5 fall within or

W_0	Mode label	k	ω_{dns}	ω_{th}	σ_{dns}	σ_{th}	$\sigma_{th}^{(\infty)}$
-0.1	A1	2.30	0.349	0.347	0.0288	0.0307	0.0314
	A2	5.06	0.035	0.021	0.0173	0.0176	0.0211
	A3	7.40	0.002	-0.010	0.0266	0.0260	0.0347
	A4	9.36	-0.054	-0.068	0.0129	0.0127	0.0261
	A5	7.96	0.654	0.639	0.0242	0.0226	0.0313
	A6	10.26	0.586	0.575	0.0292	0.0287	0.0431
	A7	12.50	0.492	0.484	0.0160	0.0110	0.0330
-0.2	B1	2.92	0.181	0.177	0.0387	0.0397	0.0409
	B2	5.38	-0.067	-0.076	0.0241	0.0240	0.0288
	B3	6.04	0.512	0.494	0.0372	0.0381	0.0431
	B4	8.02	0.334	0.316	0.0227	0.0221	0.0319
	B5	9.26	0.251	0.226	0.0105	0.0090	0.0235
	B6	8.80	0.942	0.921	0.0321	0.0326	0.0431
	B7	10.62	0.774	0.751	0.0183	0.0165	0.0331
	B8	11.86	0.677	0.650	0.0073	0.0041	0.0267
	B9	11.52	1.395	1.367	0.0252	0.0254	0.0431
	B10	13.24	1.227	1.198	0.0127	0.0087	0.0338
-0.3	C1	3.10	-0.029	-0.014	0.0376	0.0384	0.0398
	C2	5.64	0.246	0.230	0.0216	0.0216	0.0263
	C3	6.00	0.141	0.123	0.0091	0.0094	0.0150
	C4	6.64	0.178	0.161	0.0076	0.0070	0.0151
	C5	7.86	0.612	0.592	0.0096	0.0087	0.0179

Table 2. Summary of the primary resonant modes obtained for $W_0 = -0.1$, -0.2 and -0.3. For each mode, the table lists the axial wavenumber k, frequency ω_{dns} obtained from DNS, theoretical frequency ω_{th}, growth rate σ_{dns} from DNS at $\mathrm{Re} = 10^4$, viscous growth rate σ_{th} from theory at $\mathrm{Re} = 10^4$ and inviscid growth rate $\sigma_{th}^{(\infty)}$ from theory.

near the corresponding ring-mode regions. Figure 15 compares the radial distributions $|u(r)|$ vs r for modes B5, B8, C2, C3, C4 and C5 – extracted from DNS via Fourier decomposition of the disturbance fields – against their corresponding eigenfunctions obtained as solutions to (4.3). This comparison shows a clear agreement between the theoretical predictions and the DNS results in capturing the ring-mode nature of these modes. As seen in the plots, the eigenfunction peaks of the m_A components (red curves) are shifted toward larger values of r, indicating that the disturbances are localised away from the vortex centre, as expected for ring modes. For a consistent comparison, the profiles are normalised by dividing all amplitudes by the maximum value of the m_A component, so that the peak of m_A equals unity. This same normalisation factor is applied to m_B for both DNS and theoretical data. Additionally, we can see from the bottom panels of (*b*) and (*c*) in figures 11 and 13 that the growth rate curves of these ring modes, i.e. B5, B8, C2-C5, are distinctly smaller in magnitude and narrower in width compared with those of core modes.

6.3. *Instability characteristics as a function of axial flow*

Having compared and validated the characteristics of the unstable modes using DNS and theory for the three discrete values of W_0, we now apply the theoretical framework to perform a more informative parametric study. In particular, we track each resonant pair continuously and examine how the mode characteristics and their growth rates evolve as W_0 varies. In this section we carry out this analysis by following each resonance $[l_A, l_B]$ for the azimuthal wavenumber pairs $(m_A, m_B) = (-1, 2)$, (0, 3), (1, 4) and (2, 5) over a continuous range of W_0 from 0 to -0.4. The results are shown for the mode pairs [1, 1],

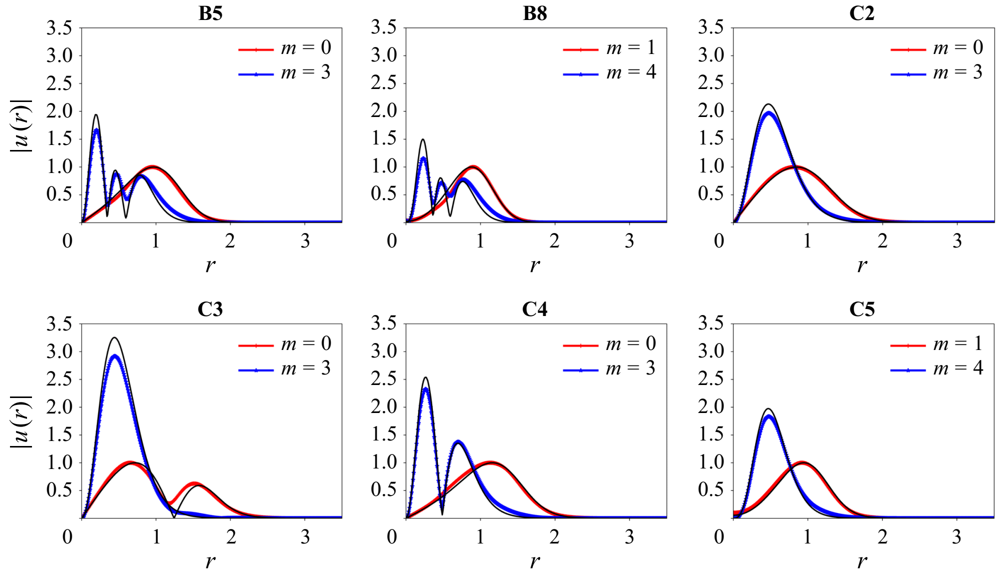

Figure 15. Distributions of the eigenfunctions $|u(r)|$ vs r for modes B5, B8, C2, C3, C4 and C5, where the modes corresponding to m_A are ring modes. Coloured lines represent DNS results, while black lines correspond to eigenfunctions obtained by solving (4.3).

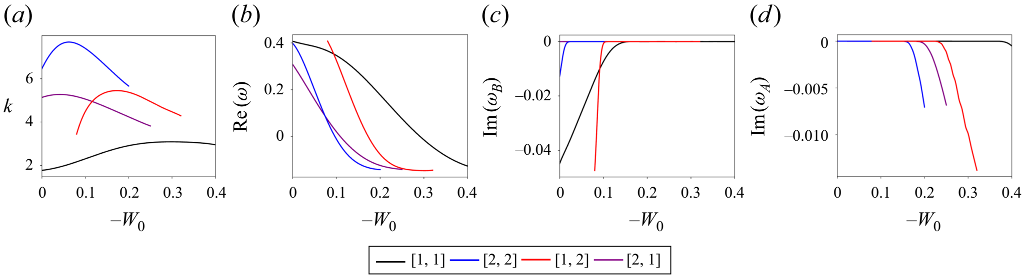

Figure 16. Characteristics of the resonant modes as a function of W_0 for $(m_A, m_B) = (-1, 2)$, corresponding to the branches $[l_A, l_B]$ indicated in the legend: (*a*) axial wavenumber k, (*b*) frequency Re(ω), (*c*) damping rate of m_B Im(ω_B), and (*d*) damping rate of m_A Im(ω_A).

[2, 2], [1, 2] and [2, 1] for all the above azimuthal combinations. For the pairs (0, 3) and (1, 4), we additionally include the results for [1, 3]. The explicit dependence of the growth rate on ϵ and Re in (6.11) also allows us to vary these parameters directly and examine how the growth rate responds. Accordingly, in the subsequent analyses, we include additional parametric studies to assess the influence of ϵ and Re on the growth rate behaviour.

The variations of the resonant axial wavenumber k, resonant frequency Re(ω) and damping rates Im(ω) for the m_B modes are plotted as functions of W_0 in panels (*a*), (*b*) and (*c*) of figures 16, 17, 18 and 19. Since the m_A modes become singular neutral only for the pair $(m_A, m_B) = (-1, 2)$ (as discussed in § 5.2), the corresponding damping rates for m_A are shown exclusively for this case in panel (*d*) of figure 16. In each figure, the values of k and Re(ω) are plotted beginning from the value of W_0 where the corresponding resonance first appears.

It can be observed that the resonances initially exhibit significant critical-layer damping for the m_B modes across all pairs. Furthermore, figure 16(*d*) shows that for $(m_A, m_B) =$

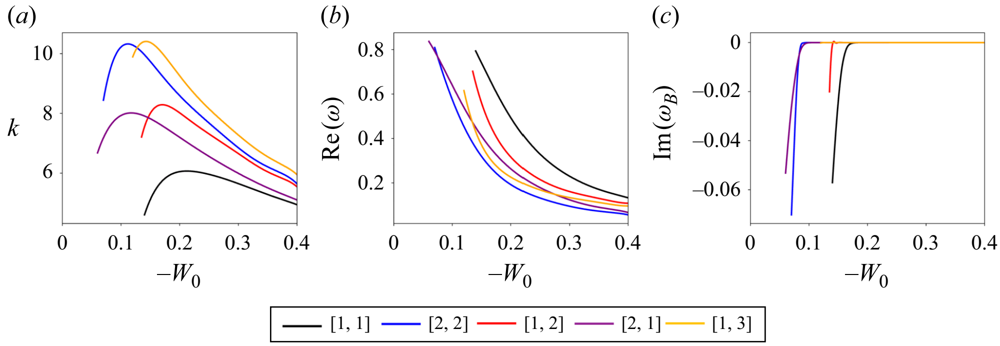

Figure 17. Same as figure 16 but for $(m_A, m_B) = (0, 3)$.

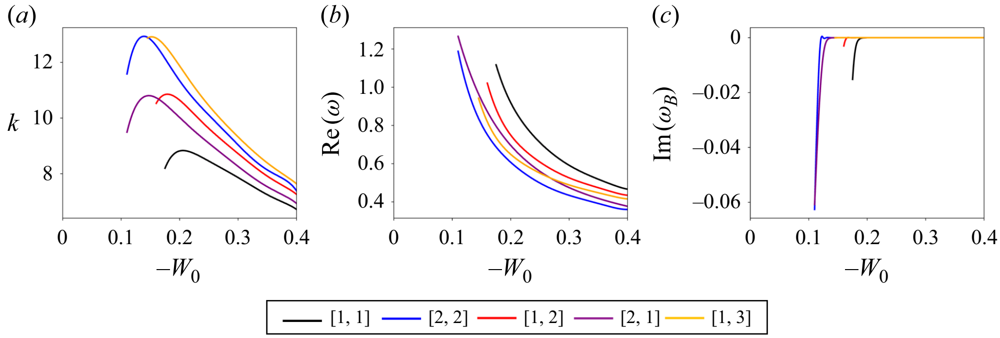

Figure 18. Same as figure 16 but for $(m_A, m_B) = (1, 4)$.

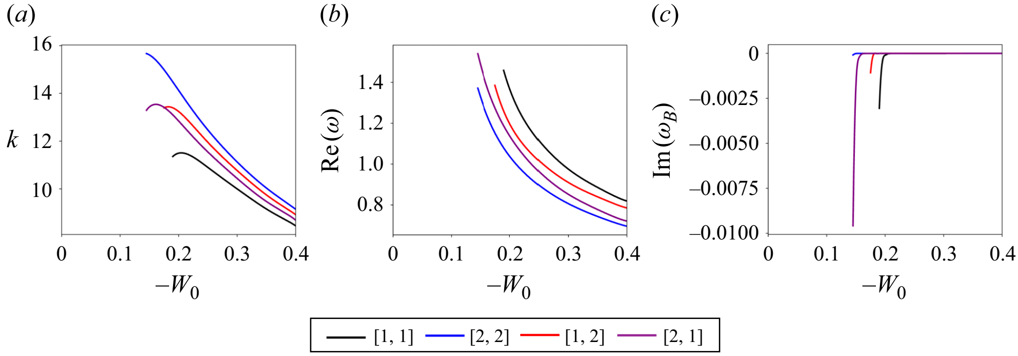

Figure 19. Same as figure 16 but for $(m_A, m_B) = (2, 5)$.

$(-1, 2)$, the modes [2, 2], [1, 2] and [2, 1] terminate as the critical-layer damping of m_A becomes significant at higher values of $|W_0|$. It is also noteworthy that the mode $(-1, 2, [1, 1])$ exhibits the most extended region of critical-layer damping across the range of W_0, from $W_0 = 0$ to approximately $W_0 = -0.15$, as seen in figure 16(*c*). Additionally, the figures show that the resonant frequency decreases monotonically as $|W_0|$ increases, appearing to asymptotically approach lower values for all modes. This trend indicates that the modes oscillate more slowly as the axial flow strengthens. It is also noteworthy that for the pair $(m_A, m_B) = (-1, 2)$, the frequency changes sign beyond a certain value of W_0, implying that only the $(-1, 2)$ modes can become stationary for some axial flow strength.

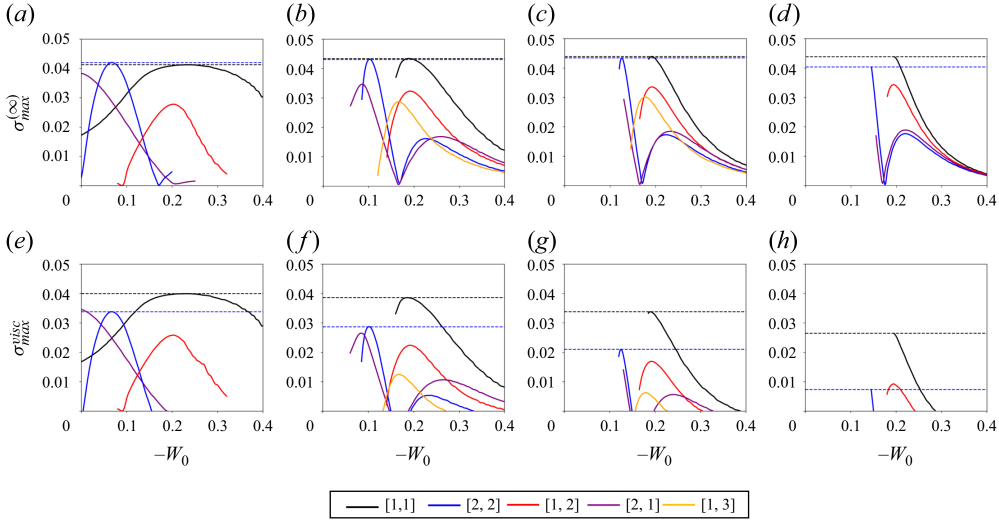

Figure 20. Panels (*a*), (*b*), (*c*) and (*d*) show the maximum inviscid growth rate as a function of $-W_0$ for (*a*) $(m_A, m_B) = (-1, 2)$, (*b*) (0, 3), (*c*) (1, 4) and (*d*) (2, 5). Panels (*e*), (*f*), (*g*) and (*h*) display the corresponding maximum growth rates at $\mathrm{Re} = 10^4$. The black dashed line indicates the maximum growth rate of the first principal mode [1, 1] and the blue dashed line corresponds to the second principal mode [2, 2].

Next, we computed the growth rates of all the above modes, using (6.11). The computation uses the eigenvalues $(k, \mathrm{Re}(\omega), \mathrm{Im}(\omega))$ and the corresponding eigenfunctions and adjoint modes at resonance, as described in § 6.1. The integrals appearing in the inner products of (6.7), (6.8) and (6.9) are evaluated along a complex contour that avoids the critical point associated with the m_B mode for all azimuthal wavenumber pairs considered. In the case of $(-1, 2)$, the contour also avoids the critical point of the m_A mode, since for certain values of W_0, even $m = -1$ exhibits a critical point on the real axis, as discussed in § 5.2. Modes that do not have a critical point are also integrated along the same contour, as the results remain unchanged.

Figure 20 shows the maximum inviscid growth rates in panels (*a*)–(*d*) and viscous growth rates at $\mathrm{Re} = 10^4$ in (*e*)–(*h*) for all modes as functions of W_0. The progressive decrease in viscous growth rates from $(-1, 2)$ to (2, 5) clearly illustrates the expected increase in volumic viscous damping with higher values of m and k. Figures 21, 22, 23 and 24 show contour plots of the growth rate magnitudes across the k bands centred around their respective resonant axial wavenumbers k_c, plotted as functions of W_0. In each figure, the left and middle panels compare the contours for the inviscid case and for $\mathrm{Re} = 10^4$ at $\epsilon = 0.008$. The right panels display the corresponding contours at $\epsilon = 0.001$, highlighting how the growth rates change under weaker straining. As observed, the growth rates become substantially smaller (scaling with ϵ^2), and the associated k bands narrow considerably when $\epsilon = 0.001$. The growth rate σ for all modes generally reaches a peak at a specific value of W_0 and then decreases as W_0 increases further.

An important observation that can be made by looking at the growth rate contours is that for several resonant modes – such as the [1, 1] and [2, 1] modes of (0, 3) in figure 22, for example, the contours begin with a sharp vertical separation at a specific W_0, where the growth rate bands are relatively wide. To the left of this W_0 value, the effective critical-layer damping, computed using (6.15) and (6.16), becomes positive near the resonant $k_c^{(\infty)}$, producing unphysical growth rate bands that are discarded. This behaviour is expected because, near this cutoff and to its left, the two Kelvin modes – when viewed on the

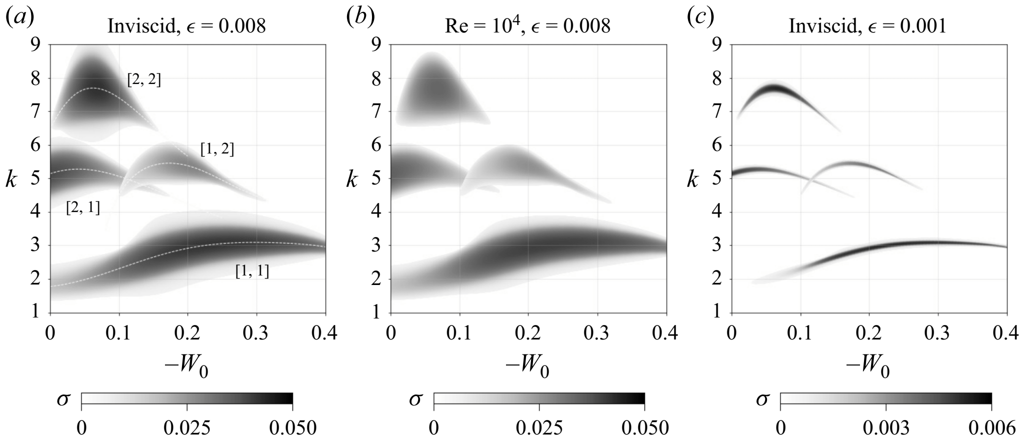

Figure 21. Growth rate σ contours on the (k, W_0) plane for $(m_A, m_B) = (-1, 2)$, corresponding to mode branches $[l_A, l_B]$ as labelled near each island. (a): inviscid case with $\epsilon = 0.008$; (b): viscous case with $\mathrm{Re} = 10^4$ and $\epsilon = 0.008$; (c): inviscid case with $\epsilon = 0.001$. The corresponding resonant axial wavenumbers as a function of $-W_0$ for those modes are also plotted as thin white dashed lines for reference.

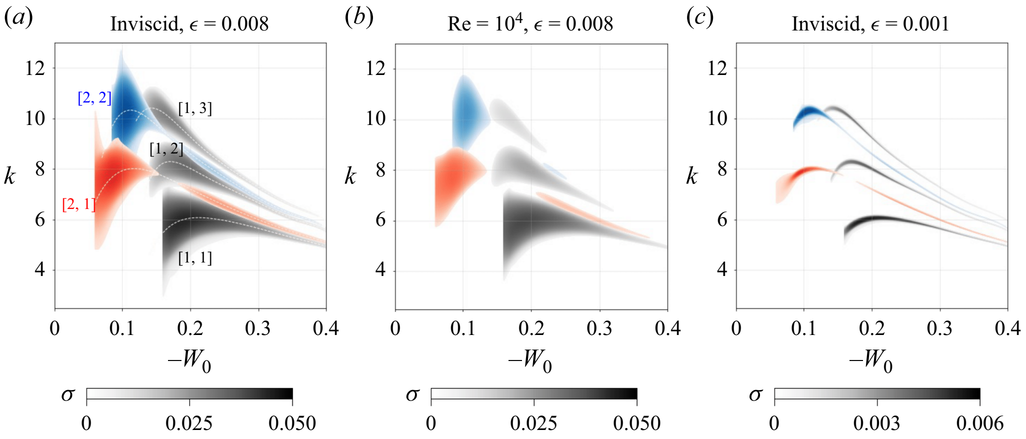

Figure 22. Growth rate σ contours on the (k, W_0) plane for $(m_A, m_B) = (0, 3)$, corresponding to mode branches $[l_A, l_B]$ as labelled near each island. (a): inviscid case with $\epsilon = 0.008$; (b): viscous case with $\mathrm{Re} = 10^4$ and $\epsilon = 0.008$; (c): inviscid case with $\epsilon = 0.001$. The modes [2, 1] and [2, 2], which exhibit two local maxima in growth rate and distinct 'tail' regions, are highlighted in red and blue, respectively, for clarity. The corresponding resonant axial wavenumbers as a function of $-W_0$ for those modes are also plotted as thin white dashed lines for reference.

dispersion curves – are nearly tangent and only barely form a crossing point. As a result, the expression for growth rate in (6.11) is not expected to give accurate values in this region unless higher-order terms are included.

Overall, the principal modes [1, 1] and [2, 2] exhibit higher peak growth rates than the other modes across all cases in the inviscid limit. This trend is consistent with previous observations for both the Rankine vortex and the elliptic instability. For illustrative purpose, in figure 25 we plot the growth rate contours for only the principal modes across all azimuthal wavenumber pairs analysed.

We shall now discuss several other interesting observations and inferences that can be drawn from these results.

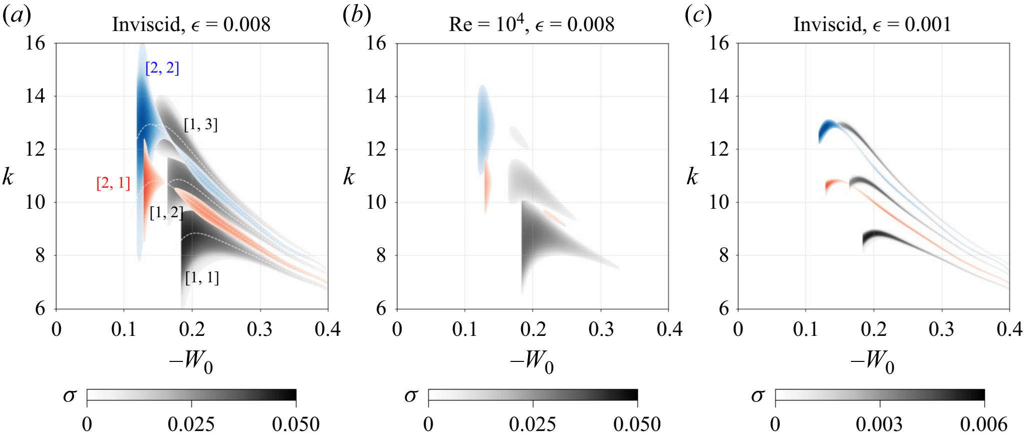

Figure 23. Growth rate σ contours on the (k, W_0) plane for $(m_A, m_B) = (1, 4)$, corresponding to mode branches $[l_A, l_B]$ as labelled near each island. (*a*): inviscid case with $\epsilon = 0.008$; (*b*): viscous case with $Re = 10^4$ and $\epsilon = 0.008$; (*c*): inviscid case with $\epsilon = 0.001$. The modes [2, 1] and [2, 2], which exhibit two local maxima in growth rate and distinct 'tail' regions, are highlighted in red and blue, respectively, for clarity. The corresponding resonant axial wavenumbers as a function of $-W_0$ for those modes are also plotted as thin white dashed lines for reference.

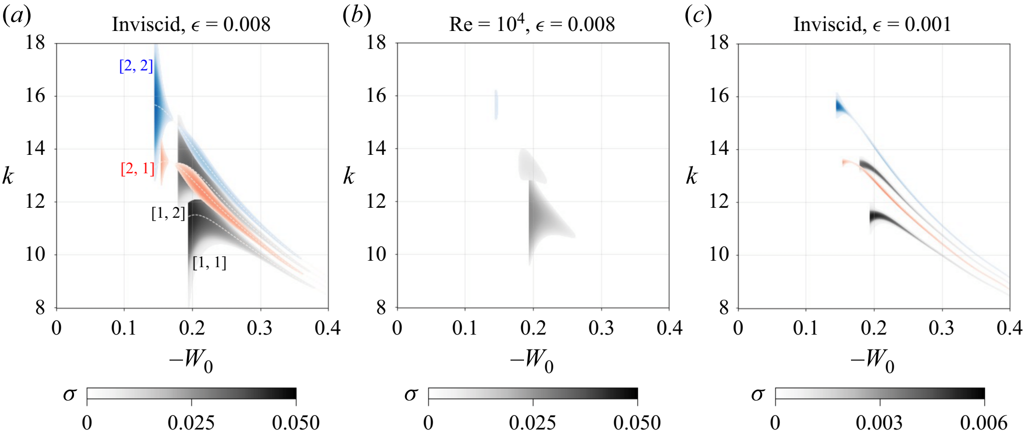

Figure 24. Growth rate σ contours on the (k, W_0) plane for $(m_A, m_B) = (2, 5)$, corresponding to mode branches $[l_A, l_B]$ as labelled near each island. Left panel: inviscid case with $\epsilon = 0.008$; centre panel: viscous case with $Re = 10^4$ and $\epsilon = 0.008$; right panel: inviscid case with $\epsilon = 0.001$. The modes [2, 1] and [2, 2], which exhibit two local maxima in growth rate and distinct 'tail' regions, are highlighted in red and blue, respectively, for clarity. The corresponding resonant axial wavenumbers as a function of $-W_0$ for those modes are also plotted as thin white dashed lines for reference.

(i) The modes corresponding to m_A in the resonant pairs (0, 3), (1, 4) and (2, 5) transition into ring modes at certain values of kW_0, as discussed in § 5.2. This transition for the modes in the present analysis is illustrated more clearly in figure 26. Interestingly, across all three pairs, the order in which the ring-mode transition occurs among the branch combinations follows a consistent pattern: [1, 3], [1, 2], [1, 1], [2, 2], [2, 1]. Modes involving the first branch of m_A are the first to undergo the transition, and the transition order is also correlated with higher branch numbers of

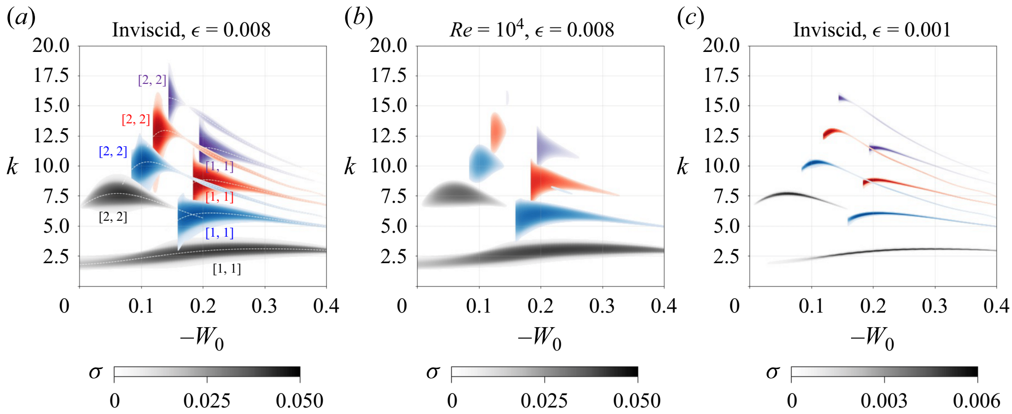

Figure 25. Growth rate σ contours on the (k, W_0) plane for the principal modes [1, 1] and [2, 2], shown for $(m_A, m_B) = (-1, 2)$ (grey), (0, 3) (blue), (1, 4) (red) and (2, 5) (purple). Left panel: inviscid case with $\epsilon = 0.008$; centre panel: viscous case with $\mathrm{Re} = 10^4$ and $\epsilon = 0.008$; right panel: inviscid case with $\epsilon = 0.001$.

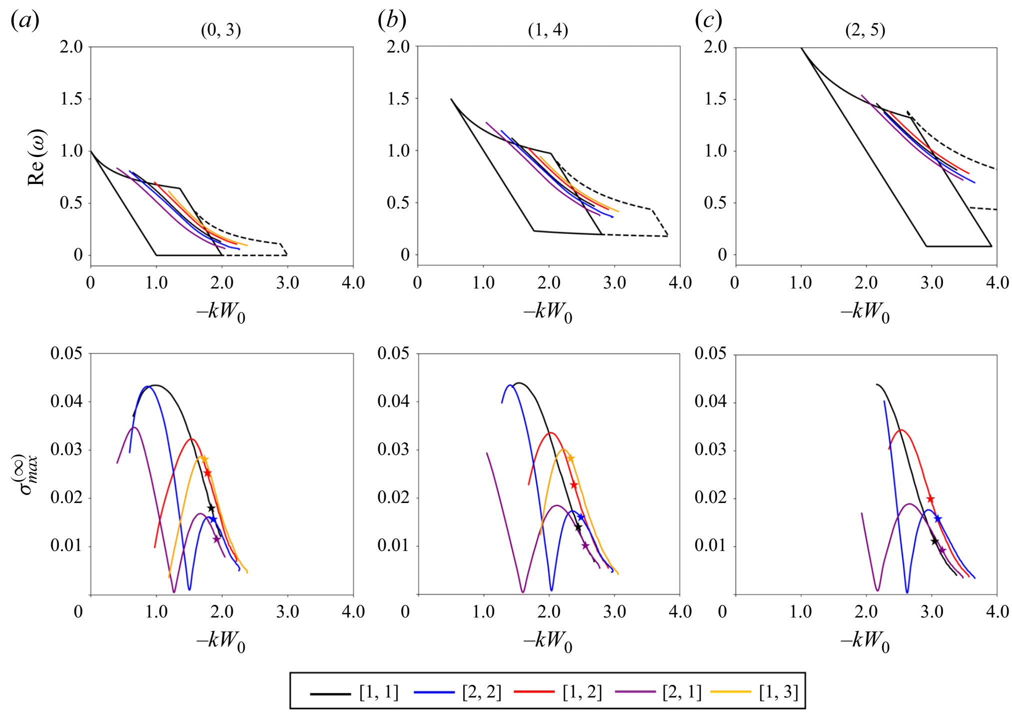

Figure 26. Transition of the modes corresponding to m_A from core modes to ring modes for (*a*) $(m_A, m_B) =$ (0, 3), (*b*) (1, 4) and (*c*) (2, 5). Top panels: frequency versus $-kW_0$ for the resonant modes, overlaid on the core and ring-mode domains predicted by asymptotic theory. Bottom panels: maximum inviscid growth rate versus $-kW_0$, with stars indicating the transition points from core to ring modes. Labels and colour scheme follow those used in figures 16–20.

m_B. As seen in the growth rate contours in figures 22, 23 and 24, these ring-mode branches are characterised by narrow, elongated k bands and relatively low growth rates.

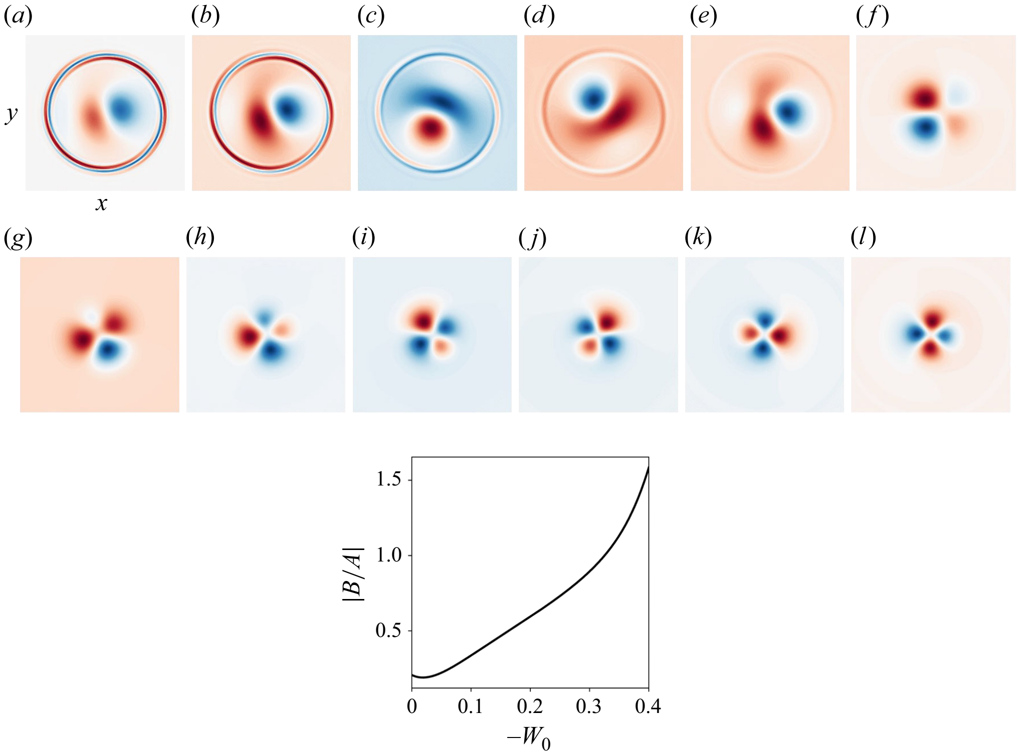

Figure 27. Top: evolution of the 2-D axial disturbance vorticity field of the mode $(-1, 2, [1, 1])$, obtained theoretically at $\mathrm{Re} = 10^4$, as W_0 varies from 0 to -0.4. Panels (*a–l*) correspond to values of $-W_0$ equal to 0, 0.025, 0.05, 0.075, 0.1, 0.15, 0.2, 0.25, 0.3, 0.35, 0.375 and 0.4, respectively. Bottom: amplitude ratio of m_B to m_A as a function of W_0.

(ii) Another interesting observation is found for the modes [2, 1] and [2, 2], where the resonance involves the second branch of m_A. For these modes, the growth rate first reaches a local maximum as W_0 increases, then drops to nearly zero and subsequently rises again to a second local maximum before eventually vanishing. This two-peak structure is not observed in modes from other branches. At first glance, one might suspect that the second peak is related to the onset of ring-mode behaviour; however, this is unlikely, as the bottom panels of figure 26 clearly show that the transition from core to ring modes occurs well after the second rise in growth. At present, we therefore do not have a definitive theoretical explanation for this peculiar feature.

(iii) We can verify from figures 20(*a*,*e*) and 21 that the Lamb–Oseen vortex results reported in AHL25 are fully recovered at $W_0 = 0$. At $\mathrm{Re} = 10^4$, only the modes [1, 1] and [2, 1] corresponding to $(m_A, m_B) = (-1, 2)$ exhibit positive growth rates, whereas the [2, 2] mode has only a very small growth rate in the inviscid limit. As expected, at $W_0 = 0$ the growth rate of the [1, 1] mode is lower than that of [2, 1], owing to the strong critical-layer damping affecting the $m = 2$ component. However, as $|W_0|$ increases, the growth rate of $(-1, 2, [1, 1])$ rises substantially, reaching its maximum for $|W_0| \approx 0.2$-0.3. This trend can be attributed to the reduction in critical-layer damping of the $m = -2$ mode, which decreases steadily and approaches zero as the axial flow magnitude increases (see figure 16*c*). This point is further illustrated by examining the evolution of the 2-D axial disturbance vorticity field of the $(-1, 2, [1, 1])$ mode. In figure 27 the top panel shows this evolution as W_0

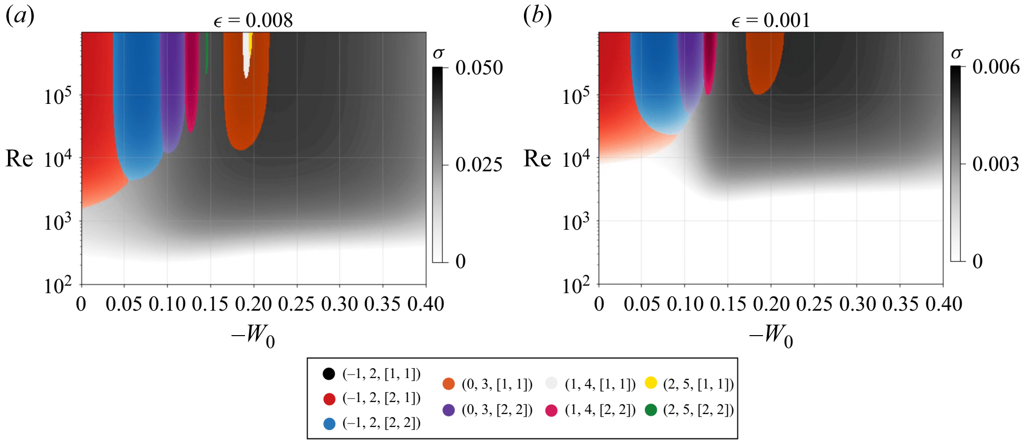

Figure 28. Contours of the maximum growth rate in the (W_0, Re) parameter space, computed for different modes identified by $(m_A, m_B, [l_A, l_B])$ as indicated in the legend. The left panel corresponds to $\epsilon = 0.008$ and the right panel to $\epsilon = 0.001$.

varies from 0 to -0.4, computed from the eigenfunctions of (4.3) at $\mathrm{Re} = 10^4$ and evaluated using (6.1) with $t = 0$ and $z = 0$. At small $|W_0|$, a clear spiral pattern – stemming from the critical-layer wave associated with $m = 2$ – is visible. As $|W_0|$ increases and the critical-layer influence weakens, the spiral gradually disappears and the mode transitions to a more regular structure. The bottom panel of figure 27 shows the associated variation of the amplitude ratio $|B/A|$ between the m_B and m_A components, computed using (6.5) or (6.6). The ratio increases monotonically with $|W_0|$, indicating growing participation of the m_B mode as its critical-layer damping decreases. Once $|W_0|$ exceeds a moderate threshold, the ratio surpasses unity, indicating that m_B overtakes m_A and becomes the dominant contributor to the mode composition.

The variation of the maximum growth rate magnitudes on Re is analysed in the Re–W_0 parameter space and shown in figure 28 for $\epsilon = 0.008$ and 0.001. It is evident that the mode $(-1, 2, [1, 1])$, corresponding to the first principal mode of $(m_A, m_B) = (-1, 2)$, dominates most of the Re–W_0 parameter space. In contrast, other principal modes only become the most unstable in limited regions, particularly at high Reynolds numbers and small values of $-W_0$, less than approximately 0.2. Beyond $W_0 = -0.2$, the mode $(-1, 2, [1, 1])$ becomes the most unstable mode again until it fades away for some value beyond $W_0 = -0.4$. Therefore, the mode $(-1, 2, [1, 1])$ clearly emerges as the most unstable, especially at larger values of W_0. To ensure the reliability of this comparison across Reynolds numbers, we restrict the upper limit of Re to 10^6. The reason is that, in principle, as one approaches the inviscid limit, modes associated with azimuthal pairs higher than $(m_A, m_B) = (2, 5)$ may also become unstable, though at much larger axial wavenumbers. By limiting the range to $\mathrm{Re} \leqslant 10^6$, such higher-order modes are expected to remain strongly suppressed by volumic viscous damping and, therefore, do not influence the trends shown in the figure.

(iv) In figure 29 we examine the variation of the maximum growth rates across the ϵ–W_0 parameter space at a fixed Reynolds number of $\mathrm{Re} = 10^4$. Three modes – $(-1, 2, [1, 1])$, $(-1, 2, [2, 1])$ and $(-1, 2, [2, 2])$ – can be seen to dominate over a broad range of ϵ. At $W_0 = 0$, the most unstable mode is $(-1, 2, [2, 1])$, which then

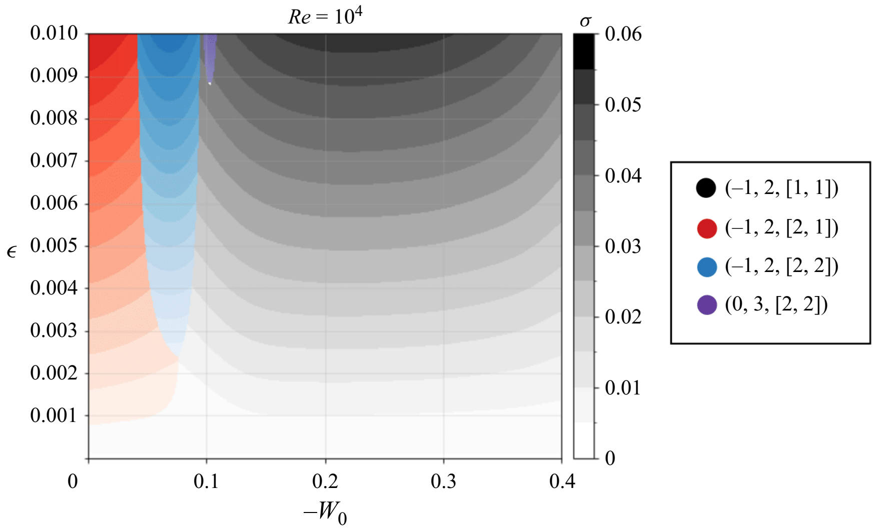

Figure 29. Contours of the maximum growth rate in the (W_0, ϵ) parameter space for Re $= 10^4$. Modes identified by $(m_A, m_B, [l_A, l_B])$ are indicated in the legend.

briefly gives way to $(-1, 2, [2, 2])$, before ultimately transitioning to $(-1, 2, [1, 1])$ as the axial flow magnitude increases. Overall, these results indicate that triangular instability at moderate Reynolds numbers (e.g. Re $\approx 10^4$ as in laboratory conditions) can persist even under very weak straining, with instability observable down to $\epsilon \approx 0.001$ and growth rates of the order of $\sigma \approx 5 \times 10^{-3}$, before becoming negligible at still weaker straining strengths.

7. Conclusions

We carried out a theoretical and numerical study of the triangular instability of a Batchelor vortex subjected to a stationary triangular strain field generated by three symmetrically positioned satellite vortices. The main aim was to examine how axial flow influences the characteristics of this instability. Theoretically, the triangular instability results from a resonant interaction between two quasi-neutral Kelvin modes of the unstrained vortex, with azimuthal wavenumbers m and $m + 3$, coupled to the background triangular strain field. A multiscale analysis of the linearised perturbation equations was used to derive the corresponding growth rate. In the numerical simulations we identified the most unstable mode by solving the linearised Navier–Stokes equations around a fixed base flow.

In our earlier study (Ayapilla *et al.* 2025), we demonstrated the existence of triangular instability and characterised it for the Lamb–Oseen vortex, where resonance was limited to the azimuthal wavenumber pair $(m_A, m_B) = (-1, 2)$ (or its symmetric counterpart), with all other pairs suppressed by strong critical-layer damping. In the present work, we showed that introducing axial flow alters the resonance behaviour and, for W_0 in the range $[0, -0.4]$, additional pairs such as $(0, 3)$, $(1, 4)$ and $(2, 5)$ also become resonant. We presented the results in two parts. (i) For $W_0 = -0.1$, -0.2 and -0.3, we computed the growth rates of unstable modes numerically and compared them with theoretical predictions for the corresponding resonant modes. The simulations were conducted at Re $= 10^4$ and $\epsilon = 0.008$, showing excellent agreement between theory and numerical simulations. We also provided the axial disturbance vorticity structures and the energy ratios of the participating modes. (ii) For a few of the resonant modes of the azimuthal wavenumber pairs $(-1, 2)$, $(0, 3)$, $(1, 4)$ and $(2, 5)$, we tracked the respective mode characteristics, including growth rates, across a continuous range of W_0 from 0 to -0.4. The key findings are summarised in the next paragraph.

In Ayapilla *et al.* (2025) the most unstable mode for the Lamb–Oseen vortex in an inviscid setting or moderately high Reynolds numbers was found to be $(-1, 2, [2, 1])$, formed by the second branch of $m = -1$ and the first branch of $m = 2$, and shown to dominate most of the (Re, ϵ) parameter space. The mode $(-1, 2, [1, 1])$ was reported to become dominant only at low Reynolds numbers. In the present work, however, we have shown that as the axial flow becomes stronger, the resonance associated with the branch pair $[2, 1]$ weakens and the dominance shifts – first to $[2, 2]$ and ultimately to $[1, 1]$ – as a consequence of the reduction in critical-layer damping. Although principal modes from other pairs such as $(0, 3)$, $(1, 4)$ and $(2, 5)$ become most unstable over limited ranges for values of W_0 less than about -0.2, the mode $(-1, 2, [1, 1])$ eventually overtakes all others and remains dominant across a broader parameter space, thus emerging as the most dominant mode. We also showed that the modes associated with m_A in the pairs $(0, 3)$, $(1, 4)$ and $(2, 5)$ undergo a transition to ring modes beyond certain values of W_0. These ring modes are marked by narrow growth rate bands in k and smaller magnitudes of growth rates.

Another useful result is that, using the asymptotic framework described in § 5.2, one can find that no possible resonant mode overlaps exist for differences in azimuthal wavenumbers greater than three. This can also be verified by observing the absence of crossing points in the dispersion curves of their Kelvin modes computed numerically. This suggests that instabilities beyond triangular instability are unlikely. While detailed numerical and experimental studies would be needed to definitively rule out higher-order instabilities due to parametric resonance, it appears reasonable to conclude that in an arbitrary 2-D Lamb–Oseen or Batchelor vortex equilibrium, elliptic instability typically arises at second-order strain and triangular instability at third-order. Therefore, elliptic instability modes are generally expected to dominate, with triangular instability modes contributing to a lesser extent. However, triangular instability can become the primary mechanism when the flow is near a third-order symmetrical state or in a perfectly third-order symmetrical configuration like the one studied here. Additionally, since our investigation is restricted to linear stability, these conclusions hold only in the absence of nonlinear effects; incorporating nonlinear dynamics could significantly alter this picture.

In this study, although small values of axial flow were considered to ensure that viscous centre modes do not become more unstable than the triangular instability modes, it is important to verify whether any viscous centre modes become unstable within the range of W_0 explored here and how their characteristics compare to those of triangular instability – particularly at higher magnitudes of W_0. Using the asymptotic theory developed by Le Dizès & Fabre (2007), it is found that in the limit of infinite Reynolds number, viscous centre modes with azimuthal wavenumber $m \geqslant 1$ are always unstable for $W_0 < 0$. These modes have axial wavenumbers approximately equal to $-mW_0$, and their growth rates scale as $Re^{-1/3}$, making them negligible at very high Reynolds numbers. However, at lower Reynolds numbers, their growth rates increase, and the critical magnitude of W_0 above which they become unstable also increases. As an example, we examine the case of $\mathrm{Re} = 10^4$ and compute the critical axial flow values beyond which viscous centre modes with $m > 0$ become unstable, using the estimates provided in Fabre & Le Dizès (2008). For $m = 1$, the critical value is $W_0 \approx -0.33$; for $m = 2$, $W_0 \approx -0.406$; and for $m = 3$, $W_0 \approx -0.541$. Therefore, within the range $-0.4 \leqslant W_0 \leqslant 0$ considered in this study, only the $m = 1$ viscous centre mode becomes unstable, and only when $W_0 < -0.33$. The numerically determined magnitude of the critical value for $m = 1$ by Fabre & Jacquin (2004) is slightly lower, at $W_0 \approx -0.31$. At $W_0 = -0.4$ and $\mathrm{Re} = 10^4$, the numerical growth rate of the $m = 1$ viscous centre mode is 0.004, whereas the most unstable triangular instability mode $(-1, 2, [1, 1])$ at the same conditions and $\epsilon = 0.008$ has a growth rate of 0.0292, which is approximately 7.3 times larger. The critical value of ϵ at which the centre mode overtakes the triangular instability mode in growth rate is approximately $\epsilon \approx 0.00135$. As for the inviscid centre modes, the condition given by Heaton (2007) indicates that they become weakly unstable only when $|W_0| > 0.433$, which lies outside the range of W_0 considered in this study.

Overall, the results of this work can have useful implications in studies concerning rotor wakes of propellers with three blades, where the hub vortex can in principle be subject to a third-order strain induced by the satellite vortices, and opening the door for potential triangular instability modes to develop in the wake of the hub vortex. Also, triangular instability can be one of the potential mechanisms, along with elliptic instability, which can be used to explain the pathways of transition to turbulence. However, several questions need to be addressed that merit further exploration in future work.

In Ayapilla *et al.* (2025) and this study, we analysed the triangular instability characteristics under a stationary strain field, where the circulations of the satellite vortices were set to cancel out their mutual rotation. However, in a general case, the circulations may differ, causing the satellite vortices to rotate around the hub vortex. Previous work by Le Dizès (2000) showed that such rotation introduces an additional critical layer in the base flow of the strained vortex. The influence of rotation on the characteristics of the elliptic instability has also been investigated in Sipp, Lauga & Jacquin (1999), Le Dizes (2000), Le Dizes & Laporte (2002).

The base flow in our model is simplified to two dimensions. However, in real rotor wakes, the tip vortices form helical structures, which generate a third-order azimuthal strain field with helical symmetry and axial variation linked to the helical pitch. Investigating how this axial dependence influences triangular instability would be a valuable direction for future work. Additionally, the hub vortex is not always aligned with the rotor axis – it can adopt a helical geometry depending on the rotor design (Durán Venegas & Le Dizès 2019). Such configurations are susceptible to additional short-wavelength instabilities, such as elliptic and curvature instabilities (Blanco-Rodríguez & Le Dizès 2016, 2017). Triangular instability may also compete with instabilities developing in the cores of the helical satellite vortices and with global long-wavelength instabilities that affect the full hub–satellite system (Quaranta, Bolnot & Leweke 2015; Durán Venegas & Le Dizès 2019). Recently, Hattori & Hirano (2024) explored the effect of pitch on the nonlinear dynamics of the long-wave instability of helical vortices. Other important studies addressing rotor wake systems comprising the hub vortex, root vortices and tip vortices include Felli, Camussi & Di Felice (2011), Sørensen (2011), Iungo *et al.* (2013), Viola *et al.* (2014), Ashton *et al.* (2016), Felli & Falchi (2018), Posa, Broglia & Balaras (2022), among others. These works have shown evidence of Widnall (1972) type instabilities in rotor wakes and determined that the stability of the hub vortex is influenced by the evolving stability of the tip vortices. Single-helix ($m = 1$) and double-helix ($m = 2$) modes have also been identified as dominant modes of the hub vortex, arising from unstable inviscid perturbations in a rotating vortex with axial flow, where stability is given by the Leibovich–Stewartson criterion. We suggest that the findings of our study, along with future extensions on triangular instability, can contribute to refining the understanding of the complex interplay of instabilities and the rich dynamics occurring in rotor wakes, with potential benefits for the design of wind farms, ship propellers and other rotating machinery.

Declaration of interests. The authors report no conflict of interest.

Appendix A. Linear stability analysis – operators and coefficients

The operators appearing in (4.1) are

$$\mathcal{L}=\begin{pmatrix}1 & 0 & 0 & 0\\ 0 & 1 & 0 & 0\\ 0 & 0 & 1 & 0\\ 0 & 0 & 0 & 0\end{pmatrix}, \tag{A1}$$

$$\mathcal{P}=\begin{pmatrix}W_0\mathrm{e}^{-r^2} & 0 & 0 & 0\\ 0 & W_0\mathrm{e}^{-r^2} & 0 & 0\\ 0 & 0 & W_0\mathrm{e}^{-r^2} & 1\\ 0 & 0 & 1 & 0\end{pmatrix}, \tag{A2}$$

$$\mathcal{M}=\begin{pmatrix}\varOmega\dfrac{\partial}{\partial\theta} & -2\varOmega & 0 & \dfrac{\partial}{\partial r}\\ 2\varOmega+r\dfrac{d\varOmega}{dr} & \varOmega\dfrac{\partial}{\partial\theta} & 0 & \dfrac{1}{r}\dfrac{\partial}{\partial\theta}\\ -2rW_0\mathrm{e}^{-r^2} & 0 & \varOmega\dfrac{\partial}{\partial\theta} & 0\\ \dfrac{\partial}{\partial r}+\dfrac{1}{r} & \dfrac{1}{r}\dfrac{\partial}{\partial\theta} & 0 & 0\end{pmatrix}, \tag{A3}$$

$$\mathcal{V}=\begin{pmatrix}\Delta-\dfrac{1}{r^2} & -\dfrac{2}{r^2}\dfrac{\partial}{\partial\theta} & 0 & 0\\ \dfrac{2}{r^2}\dfrac{\partial}{\partial\theta} & \Delta-\dfrac{1}{r^2} & 0 & 0\\ 0 & 0 & \Delta & 0\\ 0 & 0 & 0 & 0\end{pmatrix}, \tag{A4}$$

where

$$\Delta=\frac{1}{r}\frac{\partial}{\partial r}+\frac{\partial^2}{\partial r^2}+\frac{1}{r^2}\frac{\partial^2}{\partial\theta^2}+\frac{\partial^2}{\partial z^2}. \tag{A5}$$

$$\mathcal{N}=\frac{1}{2}\begin{pmatrix}N_{11} & N_{12} & 0 & 0\\ N_{21} & N_{22} & 0 & 0\\ N_{31} & N_{31} & N_{33} & 0\\ 0 & 0 & 0 & 0\end{pmatrix}, \tag{A6}$$

with

$$N_{11}=\frac{3f}{r^2}-\frac{3f'}{r}-\frac{3f}{r}\frac{\partial}{\partial r}-\frac{\mathrm{i}f'}{r}\frac{\partial}{\partial\theta}+\frac{2W_0kr^2f}{1-\mathrm{e}^{r^2}}, \tag{A7}$$

$$N_{12}=-\frac{9\mathrm{i}f}{r^2}+\frac{2\mathrm{i}f'}{r}, \tag{A8}$$

$$N_{21}=-\frac{\mathrm{i}f'}{r}-\mathrm{i}f'', \tag{A9}$$

$$N_{22} = -\frac{3f}{r^2} + \frac{3f'}{r} - \frac{3f}{r}\frac{\partial}{\partial r} - \frac{\mathrm{i}f'}{r}\frac{\partial}{\partial \theta} + \frac{2W_0 k r^2 f}{1-\mathrm{e}^{r^2}}, \tag{A10}$$

$$N_{31} = -2\mathrm{i}W_0\left(\frac{2rf + 2\mathrm{e}^{r^2}r^3 f + r^2 f'}{1-\mathrm{e}^{r^2}}\right), \tag{A11}$$

$$N_{32} = \frac{6W_0 r f}{1-\mathrm{e}^{r^2}}, \tag{A12}$$

$$N_{33} = -\frac{3f}{r}\frac{\partial}{\partial r} - \frac{\mathrm{i}f'}{r}\frac{\partial}{\partial \theta} + \frac{2W_0 k r^2 f}{1-\mathrm{e}^{r^2}}. \tag{A13}$$

Here $\overline{\mathcal{N}}$ is the complex conjugate of $\mathcal{N}$.

REFERENCES

ARENDT, S., FRITTS, D.C. & ANDREASSEN, O. 1998 Kelvin twist waves in the transition to turbulence. *Eur. J. Mech. B Fluids* **17** (4), 595–604.

ASH, R.L., KHORRAMI, M.R. & GREEN, S.I. 1995 Vortex stability. *Fluid Mech. Appl.* **30**, 317–317.

ASHTON, R., VIOLA, F., CAMARRI, S., GALLAIRE, F. & LUNGO, G.V. 2016 Hub vortex instability within wind turbine wakes: effects of wind turbulence, loading conditions, and blade aerodynamics. *Phys. Rev. Fluids* **1** (7), 073603.

AYAPILLA, A.S.P., HATTORI, Y. & LE DIZÈS, S. 2025 Triangular instability of a strained Lamb–Oseen vortex. *J. Fluid Mech.* **1016**, A9.

BATCHELOR, G.K. 1964 Axial flow in trailing line vortices. *J. Fluid Mech.* **20** (4), 645–658.

BAYLY, B.J. 1986 Three-dimensional instability of elliptical flow. *Phys. Rev. Lett.* **57** (17), 2160.

BLANCO-RODRÍGUEZ, F.J. & LE DIZÈS, S. 2016 Elliptic instability of a curved Batchelor vortex. *J. Fluid Mech.* **804**, 224–247.

BLANCO-RODRÍGUEZ, F.J. & LE DIZÈS, S. 2017 Curvature instability of a curved Batchelor vortex. *J. Fluid Mech.* **814**, 397–415.

CARNEVALE, G.F. & KLOOSTERZIEL, R.C. 1994 Emergence and evolution of triangular vortices. *J. Fluid Mech.* **259**, 305–331.

CROW, S. 1970 Stability theory for a pair of trailing vortices. *AIAA J.* **8** (12), 2172–2179.

DRITSCHEL, D.G. 1998 On the persistence of non-axisymmetric vortices in inviscid two-dimensional flows. *J. Fluid Mech.* **371**, 141–155.

DURÁN VENEGAS, E. & LE DIZÈS, S. 2019 Generalized helical vortex pairs. *J. Fluid Mech.* **865**, 523–545.

ELOY, C. & LE DIZÈS, S. 2001 Stability of the Rankine vortex in a multipolar strain field. *Phys. Fluids* **13** (3), 660–676.

ELOY, C., LE GAL, P. & LE DIZÈS, S. 2000 Experimental study of the multipolar vortex instability. *Phys. Rev. Lett.* **85** (16), 3400.

ELOY, C., LE GAL, P. & LE DIZÈS, S. 2003 Elliptic and triangular instabilities in rotating cylinders. *J. Fluid Mech.* **476**, 357–388.

FABRE, D. & JACQUIN, L. 2004 Viscous instabilities in trailing vortices at large swirl numbers. *J. Fluid Mech.* **500**, 239–262.

FABRE, D. & LE DIZÈS, S. 2008 Viscous and inviscid centre modes in the linear stability of vortices: the vicinity of the neutral curves. *J. Fluid Mech.* **603**, 1–38.

FABRE, D., SIPP, D. & JACQUIN, L. 2006 Kelvin waves and the singular modes of the Lamb–Oseen vortex. *J. Fluid Mech.* **551**, 235–274.

FELLI, M., CAMUSSI, R. & DI FELICE, F. 2011 Mechanisms of evolution of the propeller wake in the transition and far fields. *J. Fluid Mech.* **682**, 5–53.

FELLI, M. & FALCHI, M. 2018 Propeller wake evolution mechanisms in oblique flow conditions. *J. Fluid Mech.* **845**, 520–559.

FUKUMOTO, Y. & HATTORI, Y. 2005 Curvature instability of a vortex ring. *J. Fluid Mech.* **526**, 77–115.

HATTORI, Y., BLANCO-RODRÍGUEZ, F.J. & LE DIZÈS, S. 2019 Numerical stability analysis of a vortex ring with swirl. *J. Fluid Mech.* **878**, 5–36.

HATTORI, Y. & FUKUMOTO, Y. 2003 Short-wavelength stability analysis of thin vortex rings. *Phys. Fluids* **15** (10), 3151–3163.

HATTORI, Y. & FUKUMOTO, Y. 2012 Effects of axial flow on the stability of a helical vortex tube. *Phys. Fluids* **24** (5), 054102.

Hattori, Y. & Fukumoto, Y. 2014 Modal stability analysis of a helical vortex tube with axial flow. *J. Fluid Mech.* **738**, 222–249.

Hattori, Y. & Hirano, A. 2024 Effect of pitch on nonlinear dynamics of helical vortex disturbed by long-wave instability. *J. Fluid Mech.* **991**, R2.

Heaton, C.J. 2007 Centre modes in inviscid swirling flows and their application to the stability of the Batchelor vortex. *J. Fluid Mech.* **576**, 325–348.

Hopfinger, E.J. & Van Heijst, G.J.F. 1993 Vortices in rotating fluids. *Ann. Rev. Fluid Mech.* **25** (1), 241–289.

Lungo, G.V., Viola, F., Camarri, S., Porté-Agel, F. & Gallaire, F. 2013 Linear stability analysis of wind turbine wakes performed on wind tunnel measurements. *J. Fluid Mech.* **737**, 499–526.

Jiménez, J., Moffatt, H.K. & Vasco, C. 1996 The structure of the vortices in freely decaying two-dimensional turbulence. *J. Fluid Mech.* **313**, 209–222.

Kerswell, R.R. 2002 Elliptical instability. *Ann. Rev. Fluid Mech.* **34** (2002), 83–113.

Khorrami, M.R. 1991 On the viscous modes of instability of a trailing line vortex. *J. Fluid Mech.* **225**, 197–212.

Lacaze, L., Birbaud, A.-L. & Le Dizès, S. 2005 Elliptic instability in a Rankine vortex with axial flow. *Phys. Fluids* **17** (1), 017101–017101.

Lacaze, L., Ryan, K. & Le Dizès, S. 2007 Elliptic instability in a strained Batchelor vortex. *J. Fluid Mech.* **577**, 341–361.

Le Dizès, S. 2000 Non-axisymmetric vortices in two-dimensional flows. *J. Fluid Mech.* **406**, 175–198.

Le Dizes, S. 2000 Three-dimensional instability of a multipolar vortex in a rotating flow. *Phys. Fluids* **12** (11), 2762–2774.

Le Dizès, S. 2004 Viscous critical-layer analysis of vortex normal modes. *Stud. Appl. Math.* **112** (4), 315–332.

Le Dizès, S. & Eloy, C. 1999 Short-wavelength instability of a vortex in a multipolar strain field. *Phys. Fluids* **11** (2), 500–502.

Le Dizès, S. & Fabre, D. 2007 Large-Reynolds-number asymptotic analysis of viscous centre modes in vortices. *J. Fluid Mech.* **585**, 153–180.

Le Dizès, S. & Lacaze, L. 2005 An asymptotic description of vortex Kelvin modes. *J. Fluid Mech.* **542**, 69–96.

Le Dizes, S. & Laporte, F. 2002 Theoretical predictions for the elliptical instability in a two-vortex flow. *J. Fluid Mech.* **471**, 169–201.

Le Dizès, S. & Verga, A. 2002 Viscous interaction of two co-rotating vortices before merging. *J. Fluid Mech.* **467**, 389–410.

Leibovich, S. & Stewartson, K. 1983 A sufficient condition for the instability of columnar vortices. *J. Fluid Mech.* **126**, 335–356.

Lele, S.K. 1992 Compact finite difference schemes with spectral-like resolution. *J. Comput. Phys.* **103** (1), 16–42.

Lessen, M., Singh, P.J. & Paillet, F. 1974 The stability of a trailing line vortex. Part 1. Inviscid theory. *J. Fluid Mech.* **63** (4), 753–763.

Leweke, T., Le Dizès, S. & Williamson, C.H.K. 2016 Dynamics and instabilities of vortex pairs. *Ann. Rev. Fluid Mech.* **48** (2016), 507–541.

Leweke, T. & Williamson, C.H.K. 1998 Cooperative elliptic instability of a vortex pair. *J. Fluid Mech.* **360**, 85–119.

Meunier, P. & Leweke, T. 2005 Elliptic instability of a co-rotating vortex pair. *J. Fluid Mech.* **533**, 125–159.

Moffatt, H.K., Kida, S. & Ohkitani, K. 1994 Stretched vortices – the sinews of turbulence; large-Reynolds-number asymptotics. *J. Fluid Mech.* **259**, 241–264.

Moore, D.W. & Saffman, P.G. 1975 The instability of a straight vortex filament in a strain field. *Proc. R. Soc. Lond. A* **346** (1646), 413–425.

Pierrehumbert, R.T. 1986 Universal short-wave instability of two-dimensional eddies in an inviscid fluid. *Phys. Rev. Lett.* **57** (17), 2157.

Posa, A., Broglia, R. & Balaras, E. 2022 The dynamics of the tip and hub vortices shed by a propeller: Eulerian and Lagrangian approaches. *Comput. Fluids* **236**, 105313.

Quaranta, H.U., Bolnot, H. & Leweke, T. 2015 Long-wave instability of a helical vortex. *J. Fluid Mech.* **780**, 687–716.

Rossi, L.F., Lingevitch, J.F. & Bernoff, A.J. 1997 Quasi-steady monopole and tripole attractors for relaxing vortices. *Phys. Fluids* **9** (8), 2329–2338.

Schaeffer, N. & Le Dizès, S. 2010 Nonlinear dynamics of the elliptic instability. *J. Fluid Mech.* **646**, 471–480.

Sipp, D. & Jacquin, L. 2003 Widnall instabilities in vortex pairs. *Phys. Fluids* **15**, 1861–1874.

SIPP, D., LAUGA, E. & JACQUIN, L. 1999 Vortices in rotating systems: centrifugal, elliptic and hyperbolic type instabilities. *Phys. Fluids* **11** (12), 3716–3728.

SØRENSEN, J.N. 2011 Instability of helical tip vortices in rotor wakes. *J. Fluid Mech.* **682**, 1–4.

TSAI, C.-Y. & WIDNALL, S.E. 1976 The stability of short waves on a straight vortex filament in a weak externally imposed strain field. *J. Fluid Mech.* **73** (4), 721–733.

VIOLA, F., LUNGO, G.V., CAMARRI, S., PORTÉ-AGEL, F. & GALLAIRE, F. 2014 Prediction of the hub vortex instability in a wind turbine wake: stability analysis with eddy-viscosity models calibrated on wind tunnel data. *J. Fluid Mech.* **750**, R1.

WIDNALL, S.E. 1972 The stability of a helical vortex filament. *J. Fluid Mech.* **54** (4), 641–663.

XU, Y., DELBENDE, I., HATTORI, Y. & ROSSI, M. 2025 A numerical procedure to study the stability of helical vortices. *Theor. Comput. Fluid Dyn.* **39**, 15.